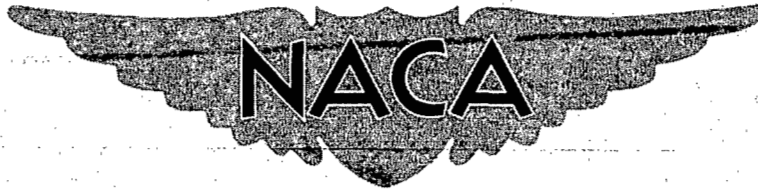


CONFIDENTIAL

Copy 6  
RM L55F29

C.2



# RESEARCH MEMORANDUM

DISTRIBUTION OF LOSSES BEHIND A COMPRESSOR ROTOR  
AS MEASURED BY A ROTATING RAKE

By William R. Godwin

Langley Aeronautical Laboratory  
Langley Field, Va.

CLASSIFICATION CHANGED  
UNCLASSIFIED

*NACA Research*

By authority of *FRN-116*

*at 7-16-57*

Date *reflective June 20, 1957*  
CLASSIFIED DOCUMENT

This material contains information affecting the National Defense of the United States within the meaning of the espionage laws, Title 18, U.S.C., Secs. 793 and 794, the transmission or revelation of which in any manner to an unauthorized person is prohibited by law.

## NATIONAL ADVISORY COMMITTEE FOR AERONAUTICS

WASHINGTON

January 17, 1956

CONFIDENTIAL

NACA RM L55F29



## NATIONAL ADVISORY COMMITTEE FOR AERONAUTICS

## RESEARCH MEMORANDUM

## DISTRIBUTION OF LOSSES BEHIND A COMPRESSOR ROTOR

## AS MEASURED BY A ROTATING RAKE

By William R. Godwin

## SUMMARY

A rotating total-pressure survey rake was employed to obtain wake measurements of a compressor rotor. The results are compared with two-dimensional cascade data of similar geometry in the form of wake distributions, total-pressure-loss coefficients, momentum-loss coefficients, and turning angles covering the Mach number range from 0.2 to 0.8. Also presented are total-pressure-loss contour plots covering the span of one blade for the angle-of-attack and Mach number range.

The results show there was considerable radial flow of the inboard-blade boundary layer and little radial flow of the inner casing boundary layer. Under conditions of low angle of attack, the mean-section losses were less than those of the cascade; these differences could not be attributed to "three-dimensional relieving." In general, the total-pressure-loss coefficients, momentum-loss coefficients, and turning angles for the rotor were in close agreement with those of the two-dimensional cascades.

## INTRODUCTION

Many axial-flow compressor designers rely on two-dimensional cascade data to select the blade profile and blade-setting angle that will produce the desired flow turning angles in the compressor's rotors and stators. This method has been very successful in spite of the fact that data obtained in a two-dimensional cascade are applied to a flow that is likely to have strong three-dimensional effects. One of the differences in blade-section performance that is commonly observed in comparing two-dimensional cascade data and three-dimensional rotor data is that the losses in the rotor are not uniformly distributed but appear to be concentrated at the hub and tip of the blades. It is, of course, assumed that radial motion of the blade boundary layer due to centrifugal forces and the interaction of the rotor blades with the boundary layers on the inner and outer casings are the primary causes of this effect, but little is known of the details of the flow pattern.

██████████

Since an analytical solution of the boundary-layer flow in this complicated flow field seems impossible, it appears that a better understanding of these flows can be obtained only by experiments.

A limited amount of information has been reported from investigations of rotating surfaces. References 1, 2, and 3 contribute data from experiments in this field. In reference 1, entire blade-section pressure distributions were measured simultaneously on a compressor rotor by means of a 24-cell pressure-transfer device. Blade-section angle of attack plotted against turning-angle curves and the pressure distributions presented were in close agreement with cascade results for the design conditions and in fair agreement for most off-design conditions except for the inboard blade section. Reference 1 also suggests reasons for the differences found at the inboard section based on tuft patterns but recommends further work in the form of wake investigations. In reference 2, Weske reports on pressure distributions and wake surveys measured on a rotating blade. In this reference, a single rotating pressure tube was mounted so as to be able to traverse the wake behind a rotating blade, or, when used in conjunction with an escapement, a single rotating-to-stationary transfer tube was used to measure a 23-point blade-section pressure distribution in sequence. Weske also presented hot-wire anemometer wake measurements and compared them with wake surveys using a single traversing static or total-pressure tube behind the rotating blade. Pearson and Grant (ref. 3) also made hot-wire measurements of rotating wakes. However, the hot wire was limited as to frequency response and wire life. In the aforementioned references there were no two-dimensional cascade wake data available for comparison with the rotor-blade wake data.

In the present report both cascade and rotor-blade wake data are presented for comparison. The wake data were obtained by using a total-pressure rake fastened to the rotor in conjunction with a multiple-cell pressure-transfer device. The surveys of the rotating blades cover the range of angle of attack and speed for 12 radial stations along the blade span. From these data the regions of high loss were easily located. By comparing data for various operating conditions, the behavior of the losses and secondary flow could be readily followed. In addition, parameters similar to those presented in cascade reports (refs. 4 and 5) are presented by using both cascade and rotating-blade data. These comparisons are intended to help the designer get better insight into the differences between blade performance in the actual rotor and in the two-dimensional cascade.

## SYMBOLS

c	chord
$C_w$	momentum-loss coefficient, $\frac{F_c}{c} \int \frac{\Delta P dw}{q_{lr}}$
dw	incremental distance across the wake
$F_c$	ratio of momentum-loss coefficient to pressure-loss coefficient
M	Mach number
P	total pressure, lb/sq ft
p	static pressure, lb/sq ft
q	dynamic pressure, $\frac{1}{2}\rho V^2$ , lb/sq ft
R	Reynolds number
r	radius
U	rotational velocity
V	velocity, ft/sec
x	location on total-pressure rake
$\alpha$	angle of attack, deg
$\beta$	inlet air angle measured to axial direction
$\theta$	turning angle
$\rho$	density
$\bar{\Delta}$	average total-pressure loss

## Subscripts:

0	entering guide vanes
1	entering compressor blades
2	leaving compressor blades

ax      axial  
m      mean section  
r      relative to blade

## TEST APPARATUS

### General Arrangement

The general equipment used for the tests described in this report was the same as that reported in reference 1 and shown in figure 1. The velocity diagram for the design condition is presented in figure 2.

The guide vanes produced a free-vortex tangential velocity distribution flowing against the direction of rotation. This was to provide high inlet Mach numbers without going to high tip speeds.

The rotor was composed of 24 blades having a uniform-loading mean line with an NACA 65-series thickness distribution and a maximum thickness of 10 percent of the chord length. The rotor blade was designed for constant spanwise power input. The layout of the blade is described in reference 1 and shown in figure 3. For these tests the main alteration to the apparatus described in reference 1 was the addition of three total-pressure rakes that were installed on the rear surface of the rotor and connected to the pressure-transfer device as the pressure blades had been in reference 1. The rakes, shown in figure 4, were located  $120^\circ$  apart for balance and were adjustable approximately 3 inches in the radial direction,  $1/2$  inch circumferentially, and  $90^\circ$  in the flow direction. Each rake covered a different radial section of the blade passage and each rake was shifted a like amount to maintain the dynamic balance of the rotor. The change in length of the connecting pressure tubing was taken care of by slip joints between the rakes and the axis of rotation.

When the first measurements were made by using the rakes it was discovered that there was a small amount of radial flow present. This radial flow caused the total-pressure tubes to be at a slight angle of attack and, hence, did not recover all the impact pressure. By drilling out the ends of the tubes as recommended in reference 6, the tubes were made insensitive to angles of incidence up to  $\pm 17^\circ$ . This greatly increased the measuring ability of the rotating rake.

The airspeed and flow direction between the guide vanes and rotor were measured with an automatic yaw instrument containing a pressure probe having null-type yaw, static, and total-pressure elements. The

probe was of the form referred to as a prism probe in reference 7 with the yaw tubes cut at a  $45^\circ$  angle for greater sensitivity.

The pressures from the rotating rakes and pressure probe were indicated on a multitube manometer and were photographed as a permanent record.

The rotor speed was measured with a Strobococonn tuning unit capable of detecting a variation in rotational speed of 0.05 percent.

For the comparison of the rotor and high-speed cascade data, some additional data were obtained from the high-speed cascade described in reference 5. The amount of wall boundary layer removed was controlled to provide a static-pressure rise through the cascade equal to that through the rotors. In other respects, the methods were the same as those reported in reference 5.

#### METHOD OF TESTING

Wake measurements were taken at the 12 radial locations shown in figure 3. The mean-section angle of attack was varied from  $8.5^\circ$  to the surge point by throttling the exiting flow. At each radial location the wakes were recorded for nine throttle settings covering the operating range for speeds of 800, 1,140, 1,600, 1,900, and 2,100 rpm. At the 17.75- and 20.00-inch radial locations, additional wakes were taken at the nine throttle settings for speeds of 900, 1,000, 1,700, 1,800, and 2,000 rpm. At each radius the rake was set at an angle equal to the design flow direction indicated by the corresponding curve of  $\alpha$  against  $\theta$  of reference 1. The rake was located circumferentially to include the entire wake as it shifted because of separation with increase in angle of attack.

#### RESULTS AND DISCUSSION

The compressor design used in these tests had guide vanes that turned the inlet flow against the direction of rotor rotation. This supplied a high-subsonic inlet relative Mach number for relatively low rotational speed. At the design angle of attack, the rotor exiting flow was axial. Thus, leaving the rotor, there is no radial static-pressure gradient to oppose the centrifugal force of the blade boundary layer. For the conventional axial-flow compressor, the guide vanes turn the inlet flow in the direction of rotor rotation. This allows high rotational velocities with subsonic relative Mach numbers. The flow leaving the rotor of the conventional compressor has a tangential

component that establishes a radial static-pressure gradient. However, this pressure gradient is insufficient to counter the effect of the higher rotational velocity of the conventional compressor. As a result, the radial unbalance of the boundary layer for the rotor of the usual axial-flow compressor will be greater than that of the rotor of this report. A calculation based on simple radial equilibrium was made of the mean-section vector diagrams at the design condition for the compressor of this report and a symmetric stage using the same geometry relative to the rotor. The results indicated that the unbalance of the radial pressure gradient of the boundary-layer air exiting the rotor was approximately eight times greater for the symmetric stage than for the reported rotor. From this it appears that the radial extent of flow of boundary layer on the usual axial-flow compressor rotor will be greater than for this rotor. In spite of this, the origins of losses and flow patterns determined in this investigation should be representative of the general rotor configuration. It would be difficult to devise a rotating rake that would be strong enough to be used at the speeds necessary to obtain the same Mach numbers relative to the blade for a symmetrical stage.

#### Variation in Total-Pressure-Loss Distribution

##### With Mach Number

Figure 5(a) shows distributions of the total-pressure-loss coefficient of the compressor-blade mean section at several Mach numbers. In this figure the wake increases in size and shifts to the left with increases in Mach number. This corresponds to the increase in separation on the upper surface of the blade with increase in local Mach number. Figure 5(b) presents cascade data for the same blade geometry as presented in figure 5(a) with the exception that the solidity is 1.25 instead of 1.18. The rake for these measurements was located slightly more than 1-chord length downstream of the blade trailing edges as compared with 0.44-chord length for the compressor. This difference accounts for the greater spread of the losses. The relative locations of the wakes are not shown as the total-pressure rake was shifted for the change in turning angle. The shape of the rotor pressure-loss profile strongly resembles a two-dimensional cascade wake profile. However, for the rotating blade, loss profiles were usually found to include additional losses that in some cases obscured the blade wake effect.

#### Variation in Total-Pressure-Loss Distribution

##### With Angle of Attack

Total-pressure-loss distributions measured by the rotating rakes are presented in figure 6 for seven angles of attack representing the

operating range. Figure 6(a) presents the section 1/2 inch out from the rotor hub. In this figure the large loss region is low-energy air from the inner casing that has moved to the low-pressure region of the root. The blade wake is practically obscured and is located as a small bulge in the loss profile in line with tube 14 at low angles of attack. As the angle of attack is increased, the low-energy air from the inner casing moves closer to the blade until near stall the blade wake is no longer discernible. At a distance of 1 inch from the rotor hub, similar profiles are found as shown in figure 6(b); here, however, the low-energy air from the inner casing has had a smaller effect on the total pressure than in figure 6(a). The mean-radius-section loss profile is shown in figure 6(c). Also shown are two-dimensional cascade-section loss profiles for corresponding geometries. The profile appears to be similar to a typical two-dimensional cascade-blade wake. There is one main difference, however, in that the loss profile becomes abnormally large with increase in angle of attack. This is the result of radial flow of the inboard boundary layer that was described in reference 1. Also noteworthy is that the wake shifts toward the upper surface with increase in angle of attack primarily as a result of increased separation on the upper surface. At the radial location 1 inch from the blade tip (fig. 6(d)), the loss distributions are found to be similar to those of the two-dimensional cascade. At this radius there is a small amount of outer casing boundary-layer air; this is indicated by the losses at the ends of the distribution. As the separation increases on the upper surface, the wake shifts and broadens. At a distance of 1/2 inch in from the blade tip (fig. 6(e)), the loss profile is still similar to the two-dimensional cascade wake with additional losses present. The additional losses are the result of the blade-tip scraping effect on the outer casing boundary-layer air. These losses are found on the left side of the figure. Here the casing loss appears to shift away from the blade with increase in angle of attack. This is contrary to the condition at the blade root (figs. 6(a) and (b)) and seems to indicate that the viscous effect in connection with the outer casing was stronger than the static-pressure gradient in influencing the boundary-layer flow on the outer casing.

### Contour Plots

Variation with angle of attack.- In order to obtain an overall spanwise picture of the flow leaving the blades, the loss distribution from the various spanwise locations was combined and plotted as contour maps having lines of constant total-pressure loss as a percent of the entering dynamic pressure.

Figure 7 presents total-pressure-loss contours for the NACA 65-(12A<sub>10</sub>)10 compressor blade in a solid-wall cascade (previously unpublished). The low-energy air on the wall was influenced by the passage



static-pressure gradient and flowed toward the low-pressure area of the blade upper surface. The blade-to-blade static-pressure gradient and the spanwise velocity gradient at the wall caused the low-energy air to roll up into a vortex as it passed through the blade row and traveled downstream. This is illustrated in figures 22 to 28 of reference 8.

In figure 8 the total-pressure-loss contours are presented for the rotor and show the variation in loss across the span with change in angle of attack at 800 rpm. The Mach numbers presented in this and similar figures are the mean-section inlet Mach numbers. For this compressor configuration (a free-vortex guide vane turning the air into the rotor), the Mach number at the outboard section is up to 3 percent greater, and at the inboard section it is up to 5 percent less than the mean-section value for low angles of attack. For high angles of attack the Mach number variation is less than 1 percent. In each figure there are three major loss regions: one at the root or hub of the rotor, one on the outer casing, and one behind the blade representing its wake.

The distribution of loss at the hub is similar to that shown for the solid-wall cascade. There is an additional concentration of boundary-layer air at hub because of the shaving effect of the rotor on the inner casing boundary layer: this air also flows across the hub toward the preceding blade's suction surface. A small amount of this low-energy air that originated near the succeeding blade may have reached the low-pressure surface and then have been centrifuged in the separated region of the blade near the trailing edge. This type of flow is shown clearly in figures 5(c), 8, 16(a), and 20 of reference 8 and in figures 3(b), 4(a), 7, and 11(a) of reference 9.

The loss region on the outer casing is the outer casing boundary-layer air that has been scraped off of the casing by the blade. The viscous forces in the wall boundary layer dominate over the blade-to-blade static-pressure gradient, thus holding the low-energy air against the blade. Some of this air is forced through the tip clearance and the remainder flows along the blade's pressure surface and is shed at the trailing edge, forming the loss region shown in the contour plot.

The third high loss region is that of the blade wake, which spans the annular passage. At the lowest mean-section angle of attack (fig. 8(a)), the wake is uniform across the entire passage. As the angle of attack increases, the inboard portion of the wake appears to shift radially out toward the mean section. This was previously indicated by the high inboard turning angles and the tufts on the blade surfaces reported in reference 2. This portion of the wake was the result of separation on the upper surface at the leading edge of the root section, resulting in a thinning of the wake at the inboard section and a thickening farther out. The increase in shift with increased angle of attack is attributed to a reduction in the radial static-pressure

gradient because of the reduction in tangential velocity of the incoming air.

As the angle of attack increases, the inboard vortex increases in strength, moves closer to the blade wake, and moves away from the rotor hub under the influence of the increased blade-to-blade gradient and the reduced radial static-pressure gradient.

The loss region on the outer casing reduces in strength with increase in angle of attack and appears to move slightly farther from the blade wake.

Variation with speed at design.- The variation in the loss-distribution contour plots with speed for the design angle of attack is shown in figure 9. As the Mach number increases, the loss at the rotor hub increases areawise but has little change in maximum value: the high losses in the blade wake increase in maximum value and areawise as well. The tip loss has a slight area increase and a slight shift away from the blade. The irregularity of contours for the  $M = 0.367$  plot are not plotting errors but are the result of some phenomenon of the flow. These irregularities were also noticed as jogs in the rotor exiting air angle.

Variation with speed for a below-design angle of attack.- For the below-design condition, the drive-motor power requirements limited the operating range to a mean-section angle of attack of about  $11.5^\circ$  at 2,100 rpm. Figure 10 presents the total-pressure-loss contours for an angle of attack of approximately  $11.5^\circ$  at several speeds. As the speed increased, the hub loss increased in both maximum value and area covered. In addition to an increase in area and maximum value, figure 10 indicates a slight shift of the inboard wake toward the mean section. The tip loss appears to shift slightly away from the blade and to increase slightly in area and maximum value.

For the above-design condition, near surge, the loss-contour variation with speed is shown in figure 11. The hub loss increases in magnitude in both area and maximum value. The high loss in the blade-wake spreads to the outboard section. The tip loss appears to shift slightly farther from the blade and to increase slightly in area and maximum value.

For intermediate conditions of speed and angle of attack not shown, the trends are continuous.

#### Spanwise Variation in Total-Pressure-Loss Coefficient

The integrated mean total-pressure losses across the blade passage at each radius are compared with two-dimensional cascade data interpolated

to the same geometry. The results are shown in figure 12 for 1,140 rpm at three angles of attack covering the operating range. In figure 12(a), the below-design condition, the mean-section angle of attack is  $8.8^\circ$ . The losses in the compressor are slightly less than in the two-dimensional cascade at the center of the span, and the losses at the walls are much higher for the rotor. As the angle of attack is increased to the design condition, the inboard blade boundary-layer air flows radially from the rotor toward the center of the span as can be seen from figure 12(b), the design condition. At higher angles of attack the radial shift is greater.

The near-surge condition is shown in figure 12(c): the radial flow has extended the inboard losses mostly to the mean section and to a lesser extent to the outboard region with all section losses greater for the compressor than for the two-dimensional cascade.

#### Variation of Low-Speed Momentum Loss Coefficient

##### With Angle of Attack

For a direct comparison of wake parameters from the compressor and published low-speed cascade data, the rotor low-speed total-pressure-loss distributions were integrated and converted to momentum-loss coefficients for the three main blade sections (outboard, mean and inboard) by the method of reference 10. For comparison, the low-speed momentum-loss coefficients are plotted against angle of attack for the three blade sections with interpolated cascade data from reference 4 of the same blade geometry (fig. 13). As was shown in figure 6(d), the outboard-section loss distribution included a small amount of outer casing boundary layer which prevented the free-stream portions from reaching zero loss. In figure 13(a), the flagged symbols represent overall values and the plain symbols represent wake losses without the casing boundary-layer losses. The overall momentum-loss coefficient for the outboard section diminished with increase in angle of attack but remained greater than the cascade values. The outboard momentum-loss coefficient without the wall boundary layer increased slightly with increase in angle of attack but remained less than the cascade values. Hence, the outer casing effect appears to diminish with increase in angle of attack.

In figure 13(b) the momentum-loss coefficient for the mean section is presented for the rotor and low-speed cascade plotted against angle of attack. Here the rotor momentum-loss coefficient is less than the cascade coefficient up to about  $1^\circ$  below design. At this point, the values of the rotor momentum-loss coefficients increase more rapidly with angle of attack and the values become greater for the rotor than for the cascade. This increase in the size of the rotor mean-section momentum-loss coefficients is due to the increase in radial flow of

low-energy air on the blade surface with increase in angle of attack as previously described in figure 8.

In figure 13(c), for the inboard section, the low-energy air from the rotor hub is included with the wake because losses in the vortex flow partially obscured those of the wake, particularly at high angles of attack. At the lowest angle of attack, the vortex or blade-hub loss region extends out just to the inboard section, and the rotor momentum-loss coefficient is only slightly greater than the cascade coefficient. As the angle of attack is increased, the rotor momentum-loss coefficient increased steadily corresponding to the steady growth of the hub loss at the inboard section. For this section, where the major losses are not produced by the blade wake, the values of  $C_w$  may have been slightly different had the rake been constructed, skewed, and oriented to locate the tubes on a line parallel to the plane of the rotor rather than in a line normal to the stream. This would shift the tubes at one end of the rake downstream and those at the other end upstream. Although the shift would probably be too small to detect any additional losses due to mixing, the loss pattern may change with axial direction because of the radial flow of the loss regions. Such a change in rake orientation would also affect figures 6(a), 6(b), and 6(c) by making the loss profiles more nearly cyclic in form.

#### Variation of Momentum-Loss Coefficient

##### With Mach Number

For comparison with the two-dimensional high-speed cascade, the momentum-loss coefficients of the compressor were computed for compressible flow by the method of reference 10. Figures 14 and 15 present a comparison of the momentum-loss coefficients as well as turning angles for both the low- and high-speed cascades and the compressor over the Mach number range tested. For the momentum-loss coefficients at the outboard section (fig. 14), the losses from the outer case were eliminated and only the actual wake was integrated by using the free-stream value as zero loss. The low-speed cascade coefficient was interpolated from data of reference 4 and the low-speed cascade turning angle was taken from the carpet plots of reference 11. The high-speed cascade momentum-loss coefficient and turning were obtained by interpolation of data from reference 5. In the figures presented, two values of turning angle are presented for the compressor; one value is measured and the other is the same measurement corrected to the mean axial velocity as in reference 1. This type of correction is suggested for comparisons if there is an axial-velocity change in the blade row. Figure 14 represents five angles of attack covering the compressor's operating range at the outboard section from the below-design limit to the near-surge

condition. The results show close agreement between the rotor and high-speed cascade for both turning angle and momentum-loss coefficient. In each case, as the separation on the upper surface increased with Mach number or angle of attack, the coefficient increased accordingly and increased the deviation angle which corresponded to a decrease in turning. Similar comparisons were made for the compressor mean section (fig. 15). For this section (NACA 65-(12A<sub>10</sub>)10) the high-speed cascade was run to match the compressor test conditions, and interpolation of the results was unnecessary. The solidity was 1.25 for the cascade tests and 1.18 for the compressor. In addition to the two-dimensional tests, cascade tests were made to match the compressor static-pressure rise for each angle of attack and Mach number. The results of these tests are shown in figure 15; the square symbol represents the cascade tests with the pressure rise matching the compressor. At the lowest angle of attack, the rotor momentum-loss coefficient remained low over most of the Mach number range and started to rise rapidly at  $M = 0.8$ , indicating that the force-break Mach number had been reached.

A check on the ratio of throat area to critical area for this operating condition showed that the ratio was approximately constant with radius and indicated that the rotor was almost choked. The fact that the ratio was constant indicated that there would not be any three-dimensional relieving of high-velocity regions and that section data for the rotor should appear similar to that of the cascade. The cascade wake increases rapidly at low Mach numbers indicating separation on the lower surface and is confirmed by the schlieren photograph in figure 53 of reference 5. If the separation amounted to blockage of 5 percent of the cascade-throat area, then the cascade ratio of throat to critical area at  $M = 0.7$  would approximately equal the rotor ratio of throat to critical area at  $M = 0.8$ . Thus, it appears that, for the mean section at this low angle of attack, the comparable cascade is more severely separated on the lower surface than the rotor and, although the reason is unknown, it is not due to the three-dimensional relieving effect.

In figure 15(b) the angle of attack is  $1^\circ$  below design. Here the rotor and cascade wake coefficients are about equal over the Mach number range. Because of the radial flow of the inboard low-energy air, there has been an increase in the rotor wake over that measured at the lower angle of attack (fig. 15(a)). This radial flow is even more evident for the design angle of attack shown in figure 15(c). The wake coefficients for the cascade reach their minimum values for Mach number range at the design angle of attack. At this angle of attack, the chordwise distribution of static pressure is relatively unpeaked for both the upper and lower surfaces, presenting less chance of separation than at other angles of attack. In figure 15(d) the cascade is near stall and is partially stalled for the two-dimensional case for all Mach numbers greater than 0.5. In this figure the blower wake coefficient

has further increased in value because of radial flow. The near-surge condition is presented in figure 15(e). At this angle of attack ( $16.8^\circ$ ), the two-dimensional cascade had difficulty in maintaining the necessary static-pressure rise and stalled at about  $M = 0.5$ , thus reducing the static-pressure rise to that of the blower and providing only partially stalled operation above  $M = 0.5$ . The rotor top speed was 2,200 rpm which limited the Mach number to 0.64 at this angle of attack. However, for the range shown in figure 15(e), the rotor wake coefficients roughly agree with those of the cascade. The turning angles for the cascade matching the blower pressure rise were higher than those for the two-dimensional cascade or the blower, thus indicating poor agreement. The turning angle for the compressor and two-dimensional cascade agreed fairly well except at high angles of attack where the compressor and low-speed cascade turning angles were lower.

### CONCLUSIONS

The compressor of this report had a free-vortex inlet flow against the direction of rotation which provided high relative Mach numbers at low rotational speed. Thus, the radial movement of boundary-layer air for this rotor is less than for the usual high-flow compressor. This does not invalidate the source nor flow direction of these losses as applied to other rotors but has simplified their detection. From an examination of the data for this rotor, the following conclusions were found:

1. There was little radial flow of the inner casing boundary layer. Instead, the low-energy air flowed from the pressure surface of one blade across the rotor hub to the suction surface of the preceding blade and was shed as it began to form a vortex.

2. At the lowest angle of attack, the blade wake was uniform across the passage. As the angle of attack increased, the inboard portion of the wake appeared to shift radially out toward the mean section. This portion of the wake was the result of separation on the upper surface at the leading edge of the root section in the casing boundary layer.

3. At the mean section, the momentum-loss coefficient for low angles of attack was less than for the two-dimensional cascade throughout the speed range. This difference could not be attributed to "three-dimensional relieving."

4. In general, the total-pressure loss coefficients, momentum-loss coefficients, and turning angles for the rotor were in close agreement with those of the two-dimensional cascades of similar geometry.

Langley Aeronautical Laboratory,  
National Advisory Committee for Aeronautics,  
Langley Field, Va., July 5, 1955.

## REFERENCES

1. Westphal, Willard R., and Godwin, William R.: Comparison of NACA 65-Series Compressor-Blade Pressure Distributions and Performance in a Rotor and in Cascade. NACA RM L51H20, 1951.
2. Weske, John R.: An Investigation of the Aerodynamic Characteristics of a Rotating Axial-Flow Blade Grid. NACA TN 1128, 1947.
3. Pearson, Carl E., and Grant, Howard P.: Quantitative Measurement of Fluctuation in Air Flow by Hot Wire Technique (Part II). Pratt & Whitney Res. Rep. No. 126, Gordon McKay Lab., Dept. Eng. Sci. and Appl. Phys., Harvard Univ., Sept. 1950.
4. Herrig, L. Joseph, Emery, James C., and Erwin, John R.: Systematic Two-Dimensional Cascade Tests of NACA 65-Series Compressor Blades at Low Speeds. NACA RM L51G31, 1951.
5. Dunavant, James C., Emery, James C., Walch, Howard C., and Westphal, Willard R.: High-Speed Cascade Tests of the NACA 65-(12A<sub>10</sub>)10 and NACA 65-(12A<sub>218b</sub>)10 Compressor Blade Sections. NACA RM L55I08, 1955.
6. Gracey, William, Coletti, Donald E., and Russel, Walter R.: Wind-Tunnel Investigation of a Number of Total-Pressure Tubes at High Angles of Attack - Supersonic Speeds. NACA TN 2261, 1951.
7. Schulze, Wallace M., Ashby, George C., Jr., and Erwin, John R.: Several Combination Probes for Surveying Static and Total Pressure and Flow Direction. NACA TN 2830, 1952.
8. Herzig, Howard Z., Hansen, Arthur G., and Costello, George R.: A Visualization Study of Secondary Flows in Cascades. NACA Rep. 1163, 1954. (Supersedes NACA TN 2947.)
9. Kofskey, Milton G., and Allen, Hubert W.: Smoke Study of Nozzle Secondary Flows in a Low-Speed Turbine. NACA TN 3260, 1954.
10. Heaslet, Max A.: Theoretical Investigation of Methods for Computing Drag From Wake Surveys at High Subsonic Speeds. NACA WR W-1, 1945. (Formerly NACA ARR 5C21.)
11. Felix, A. Richard: Summary of a 65-Series Compressor-Blade Low-Speed Cascade Data by Use of the Carpet-Plotting Technique. NACA RM L54H18a, 1954.





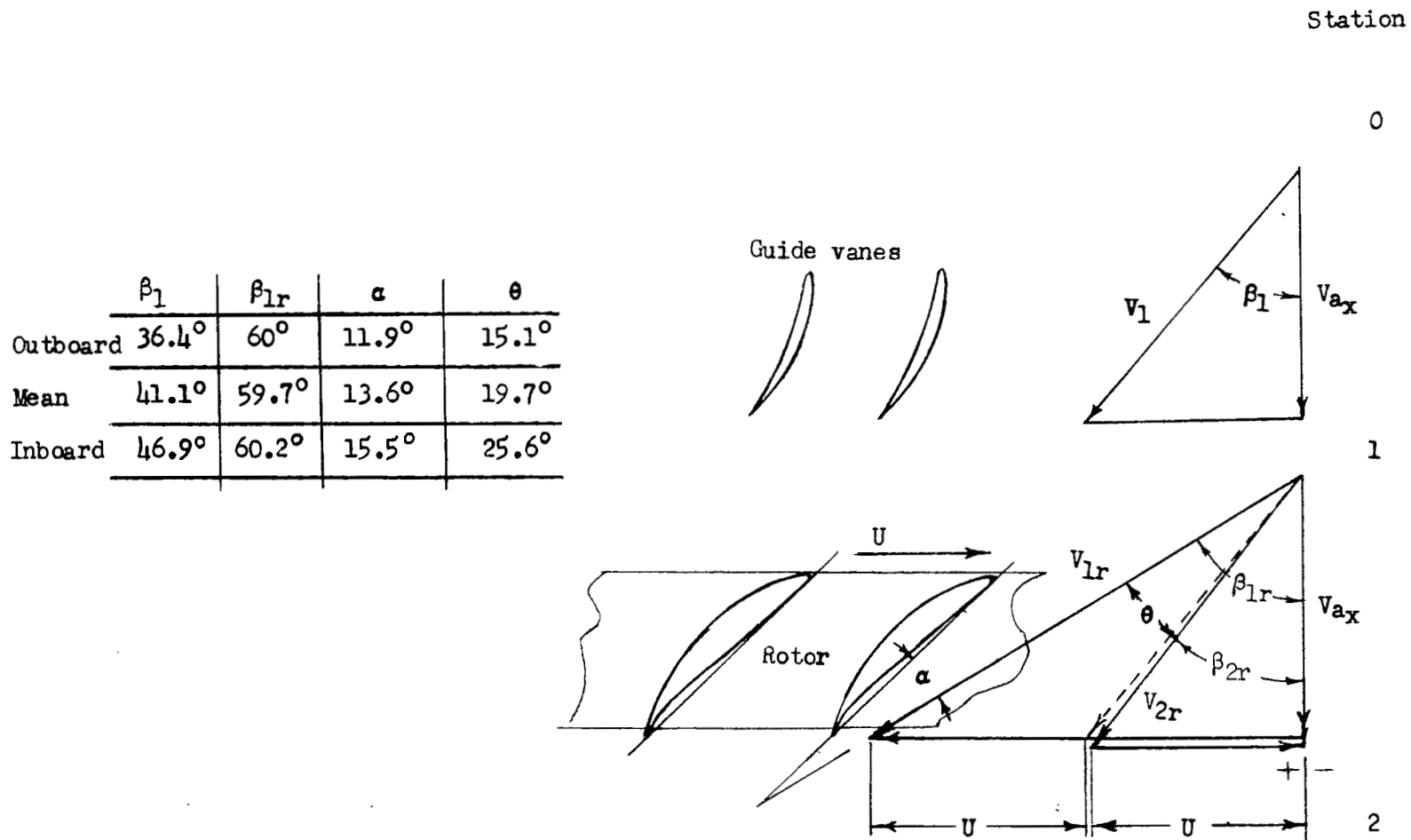


Figure 2.- Velocity diagram at design conditions.

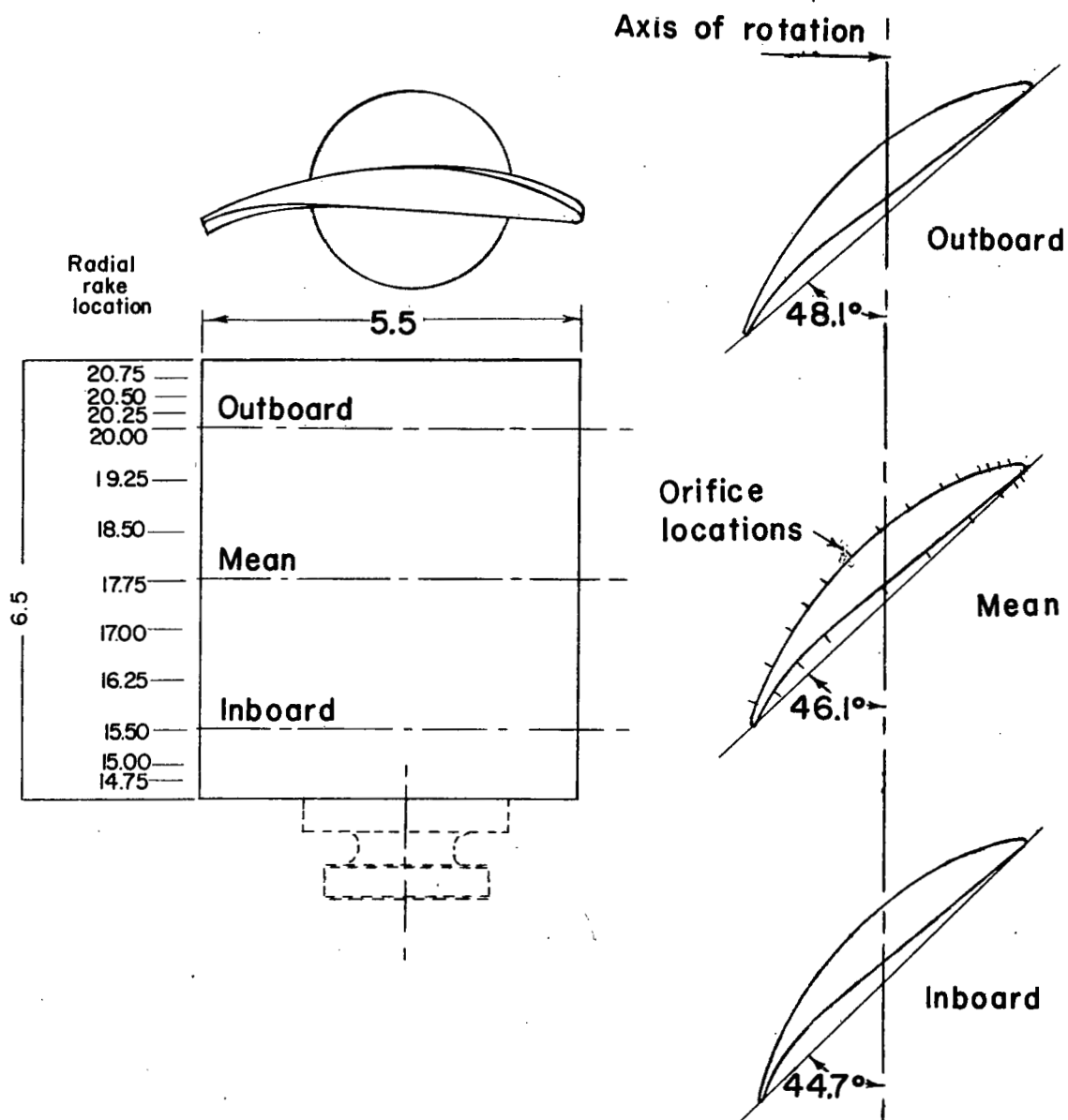
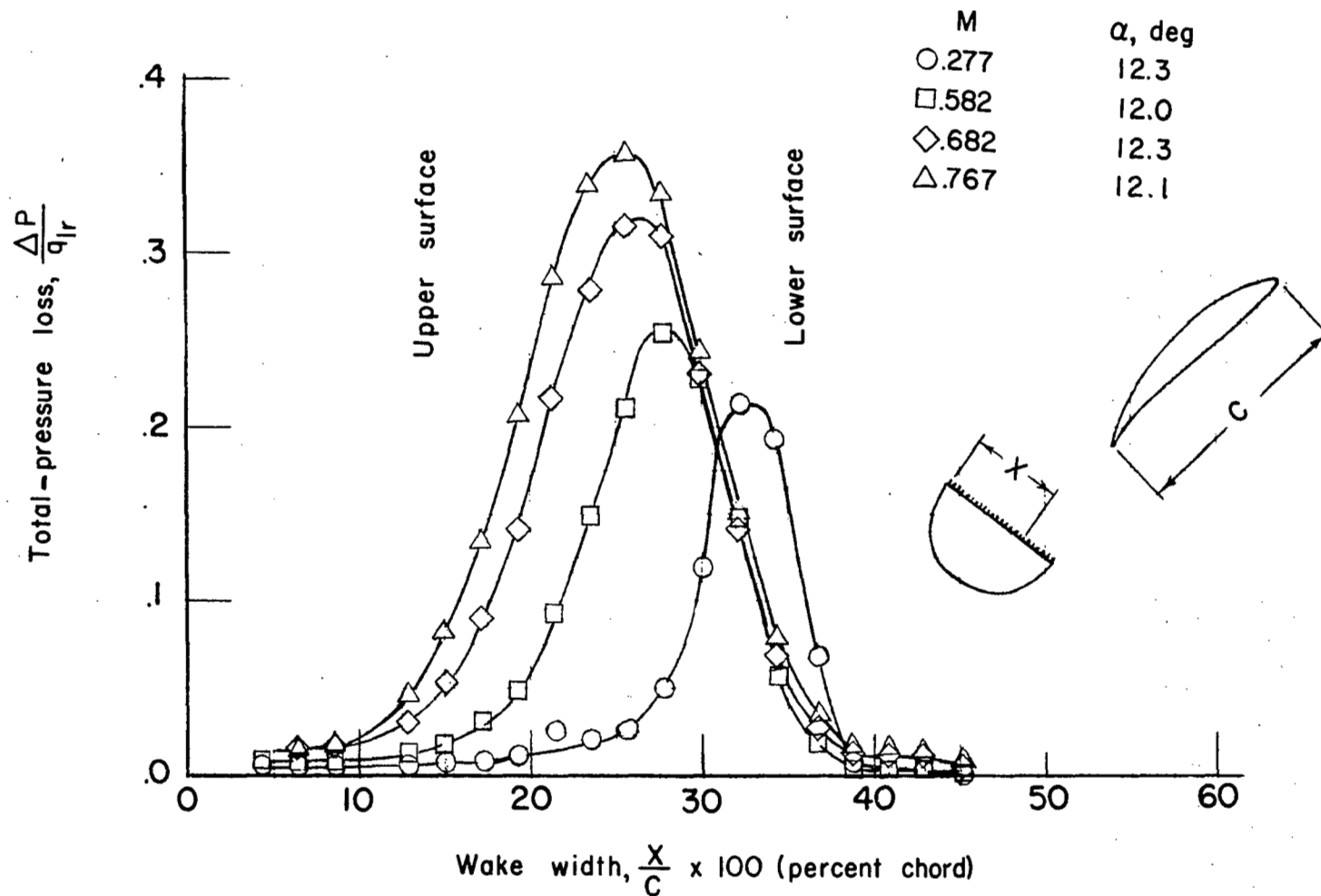


Figure 3.- Sketch of rotor blades. Linear dimensions are in inches.



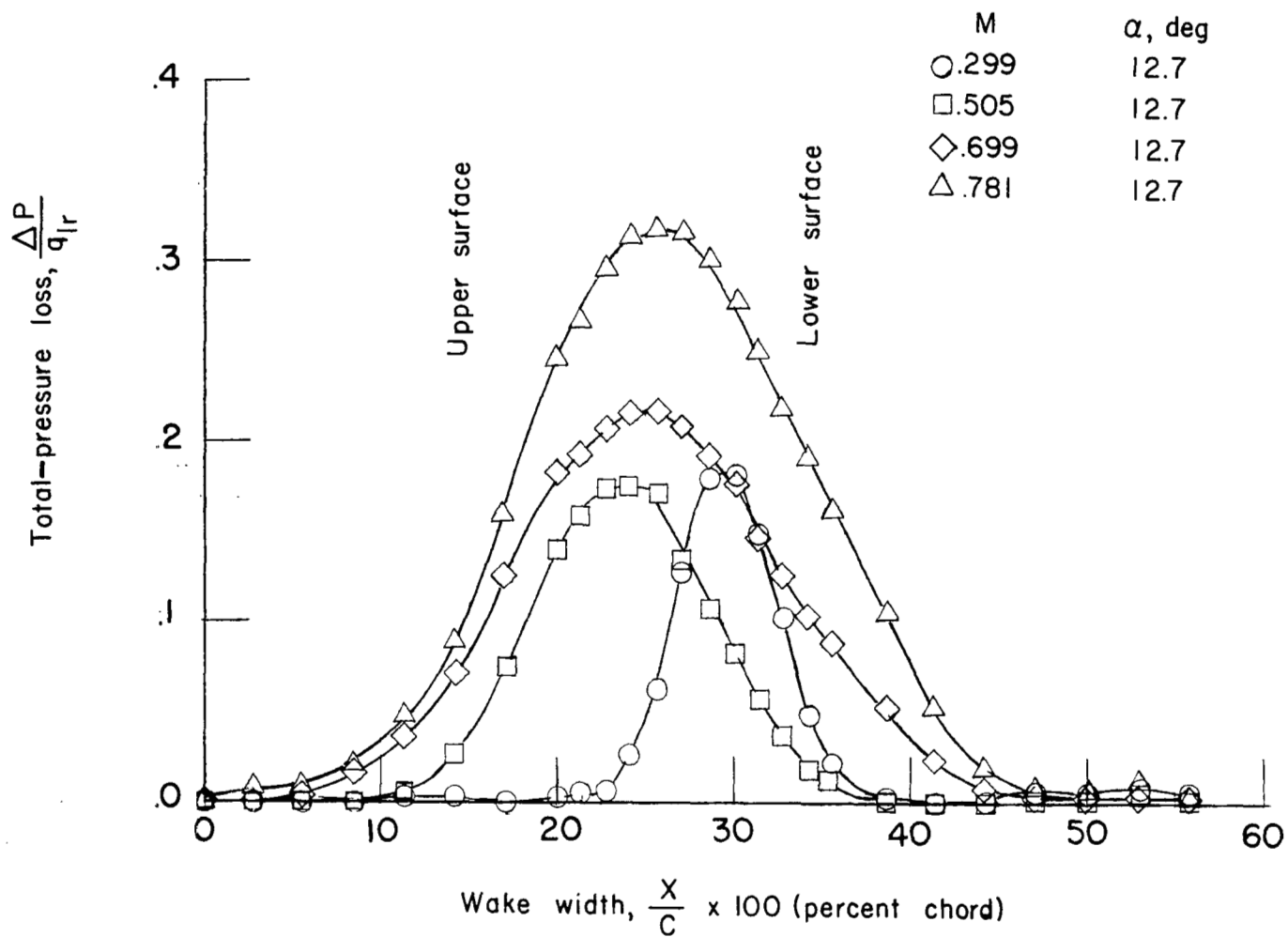
Figure 4.- Rotating rake apparatus.

L-75450



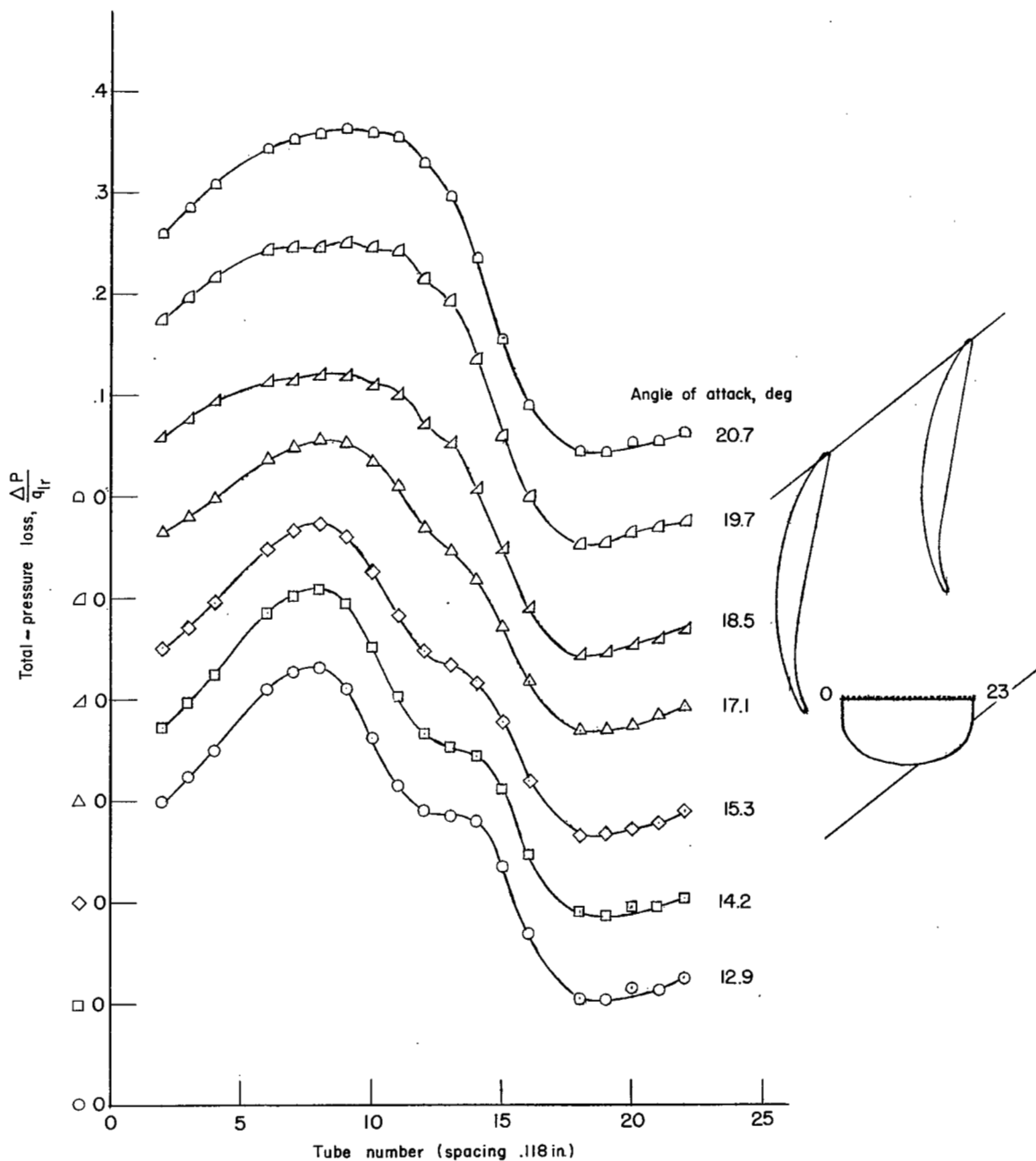
(a) The 1,000-hp compressor loss distribution for the mean section.  
 $R = 1,040,000$  to  $2,260,000$ ; rake location, 44 percent chord behind trailing edge.

Figure 5.- Loss distributions for the NACA 65-(12A<sub>10</sub>)10 blade section.



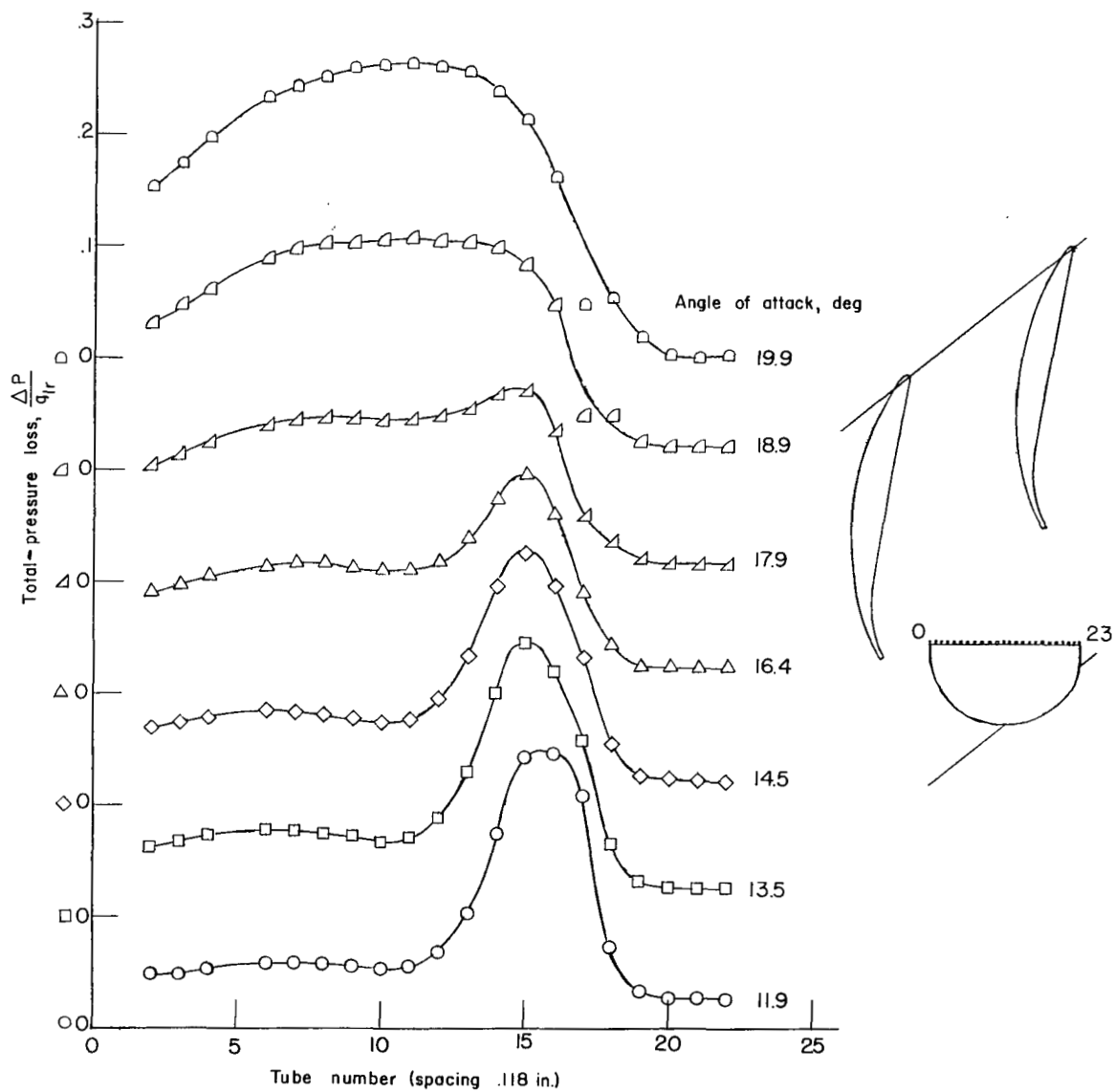
(b) High-speed cascade loss distribution.  $R = 810,000$  to  $1,510,000$ ; rake location, 120 percent chord behind trailing edge.

Figure 5.- Concluded.



(a) 15.00-inch radius.

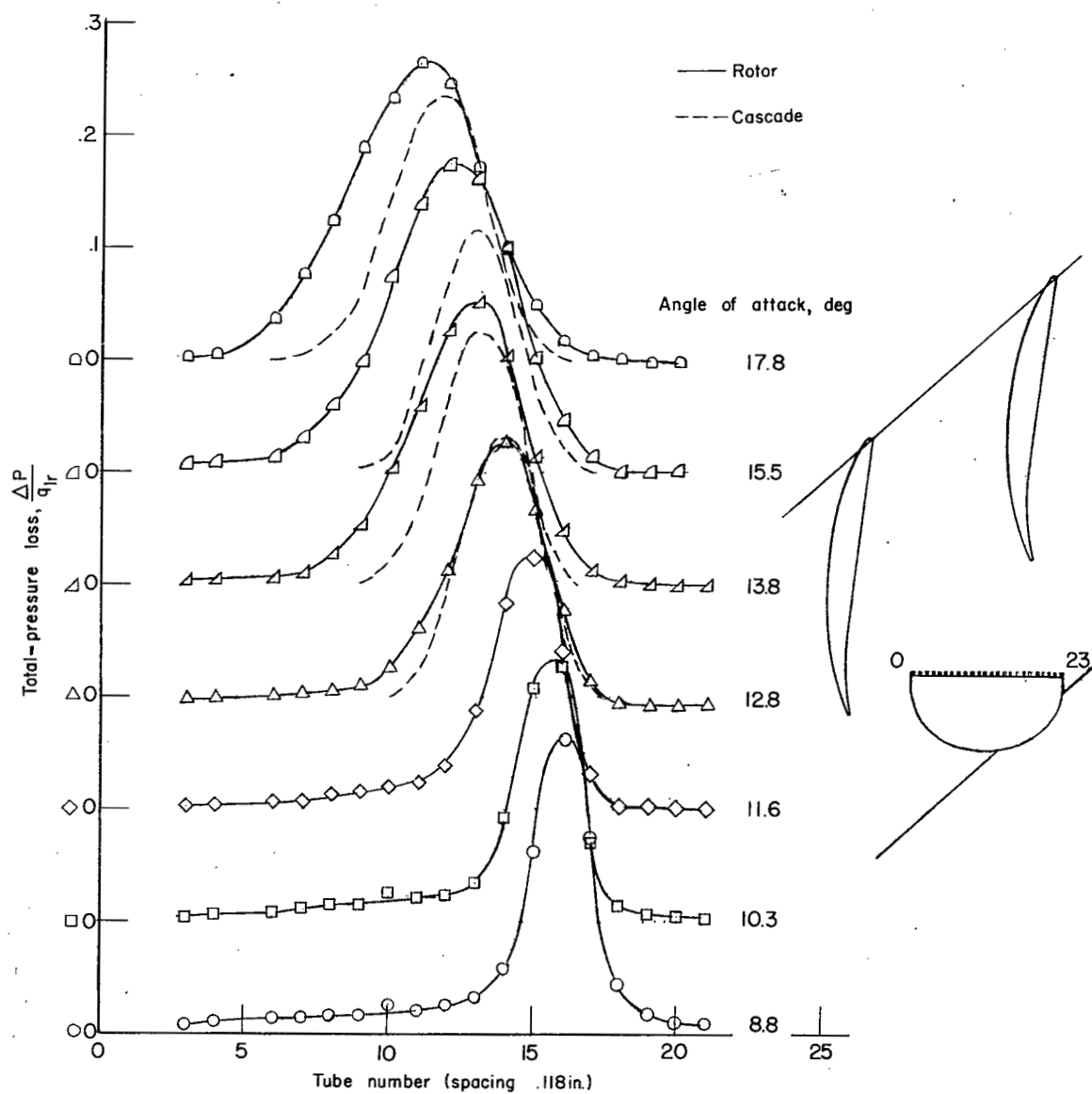
Figure 6.- Compressor total-pressure-loss distribution at various angles of attack. 1,140 rpm.



(b) 15.50-inch radius.

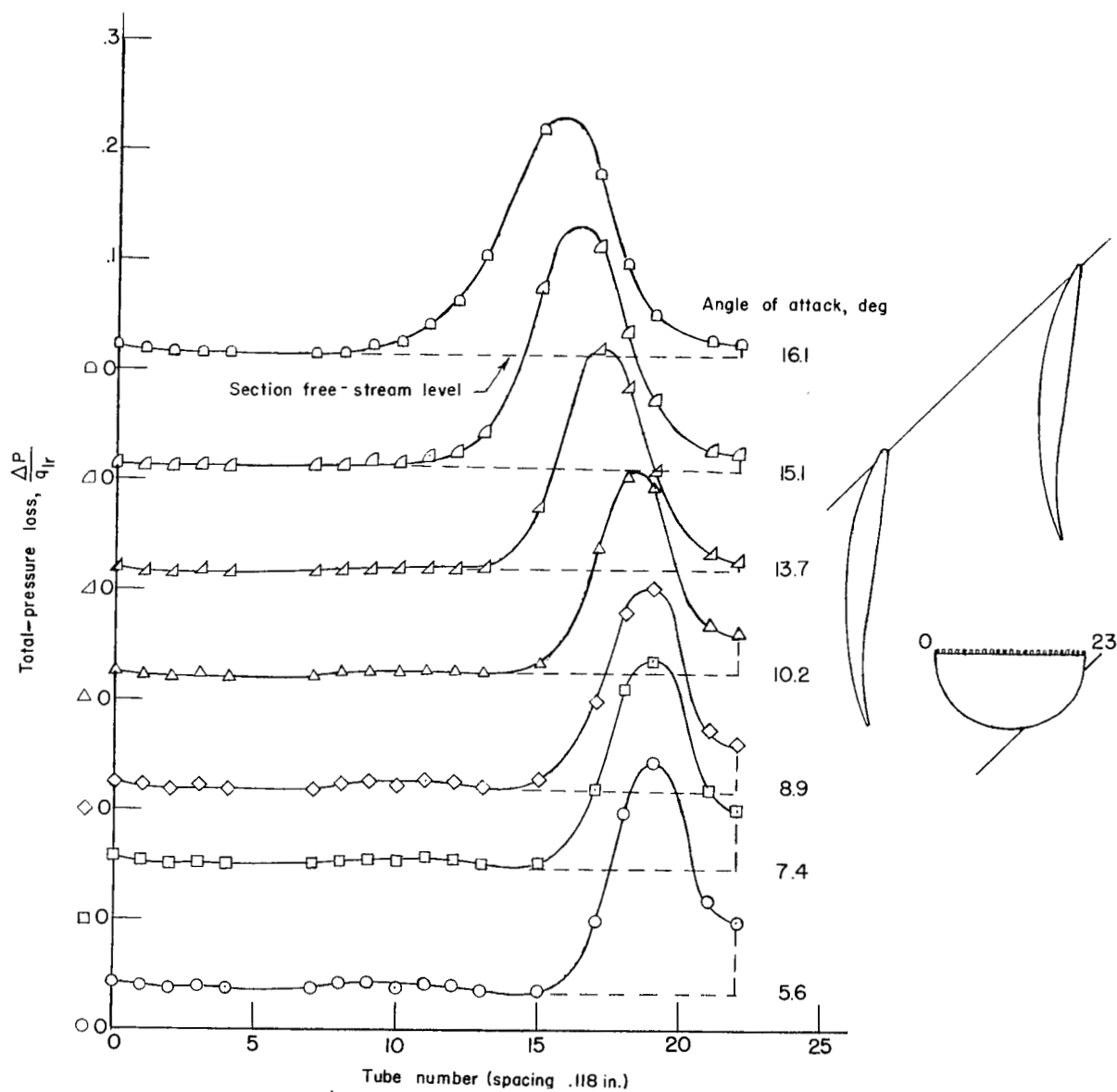
Figure 6.- Continued.





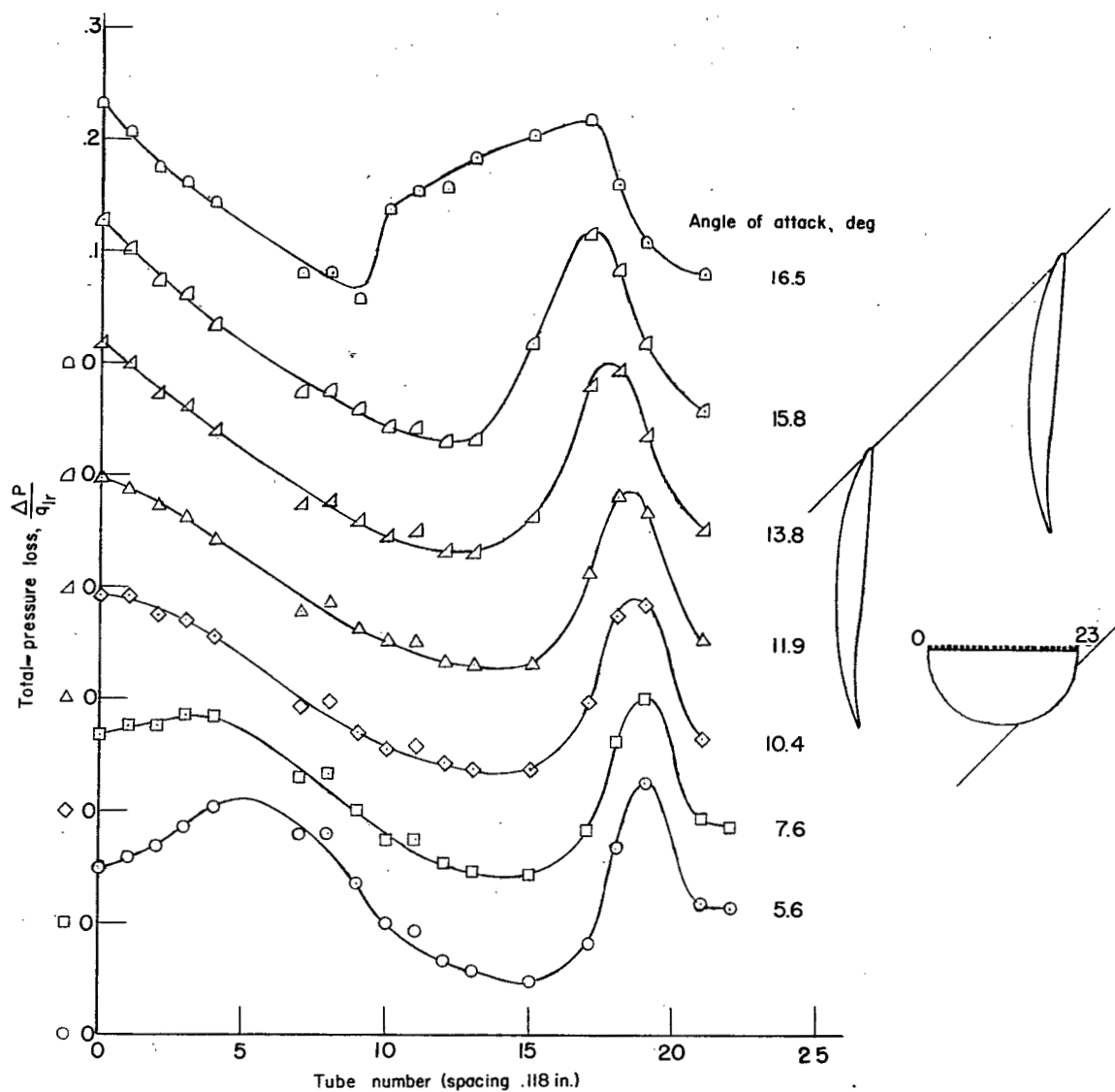
(c) 17.75-inch radius.

Figure 6.- Continued.



(d) 20.00-inch radius.

Figure 6.- Continued.



(e) 20.50-inch radius.

Figure 6.- Concluded.

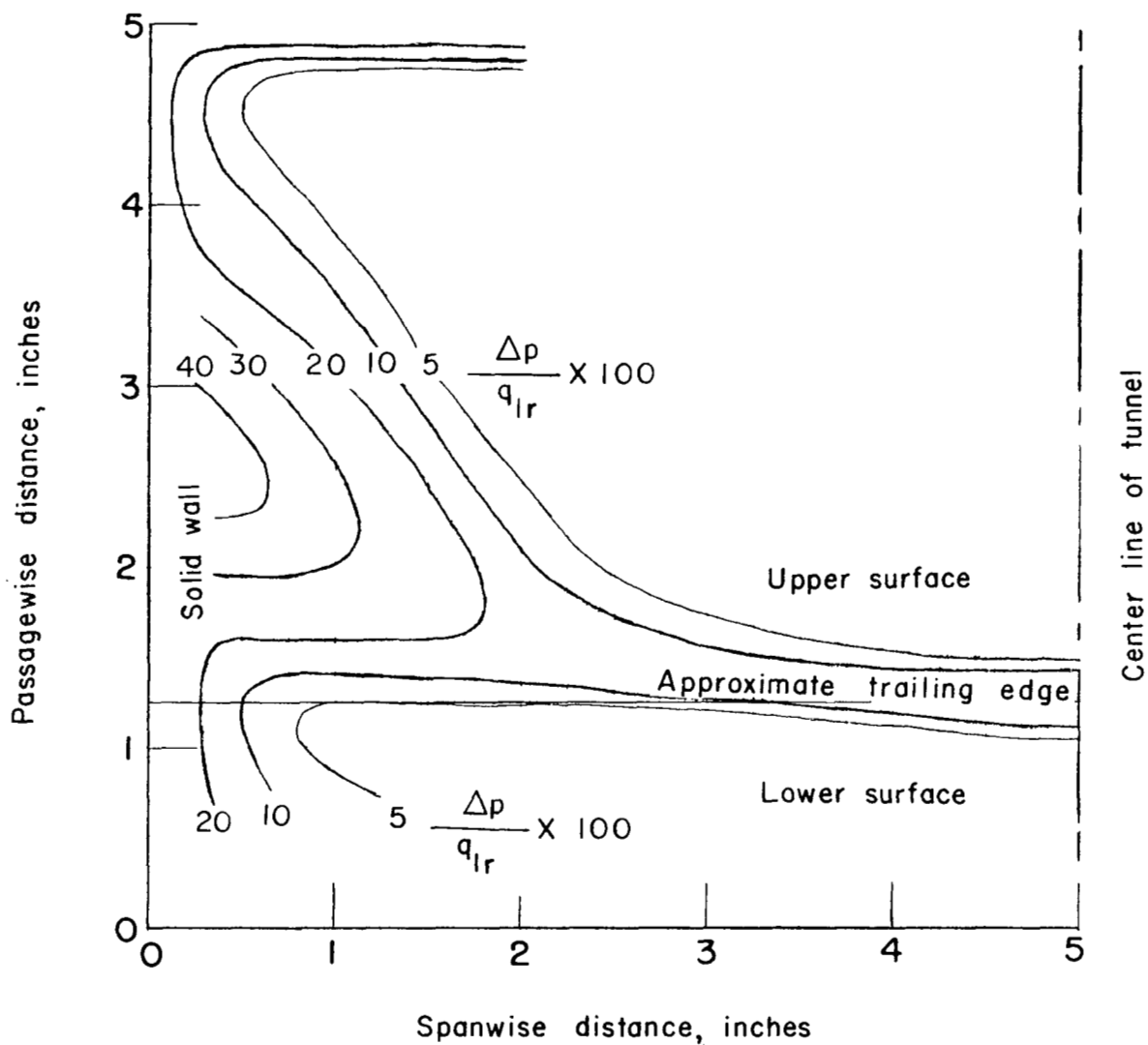
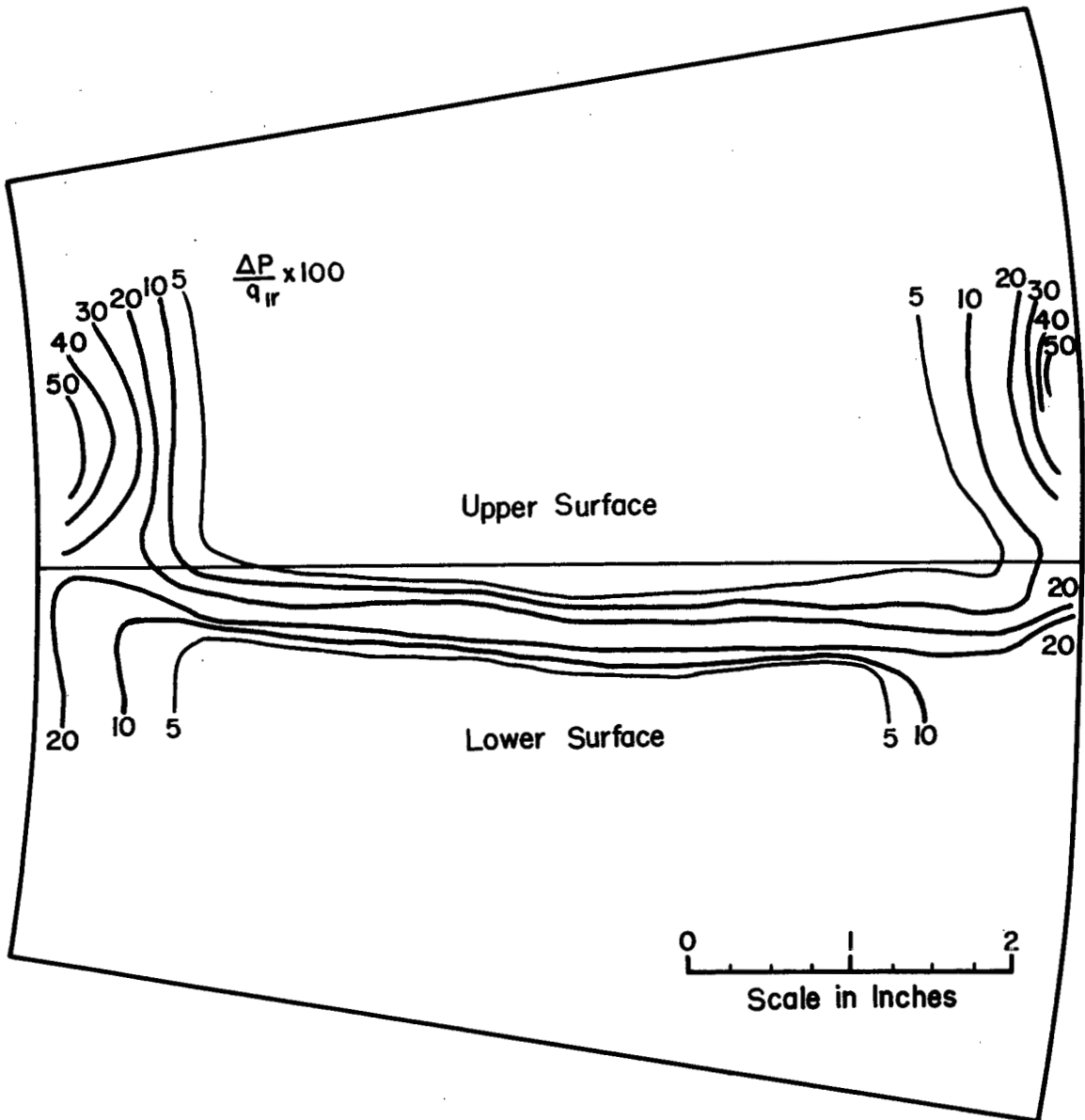
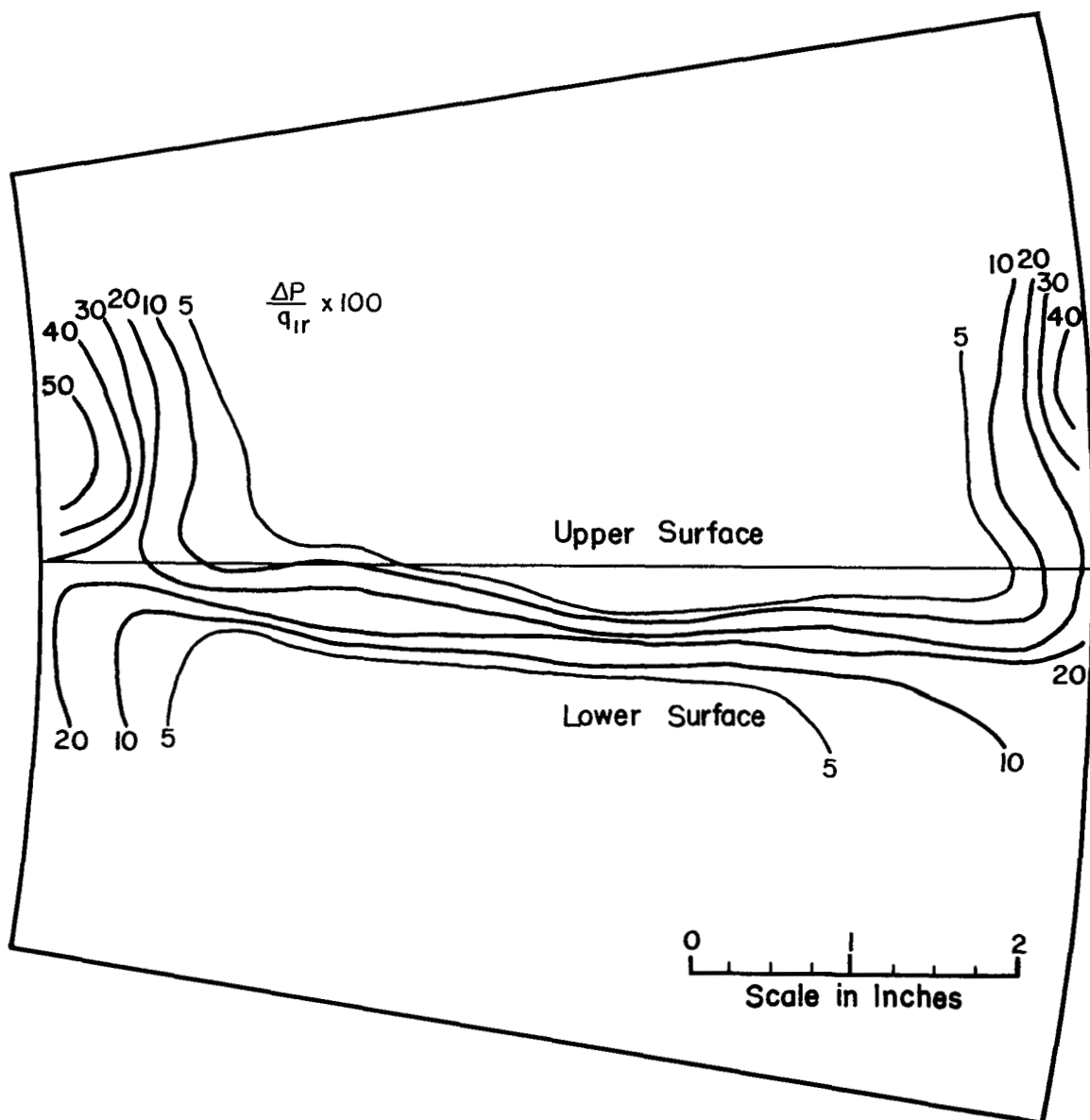


Figure 7.- Total-pressure-loss contours for the NACA 65-(12A<sub>10</sub>)10 compressor blade in a solid-wall cascade.  $\alpha = 13.2^\circ$ ;  $\beta = 60^\circ$ ;  $\sigma = 1.0$ .



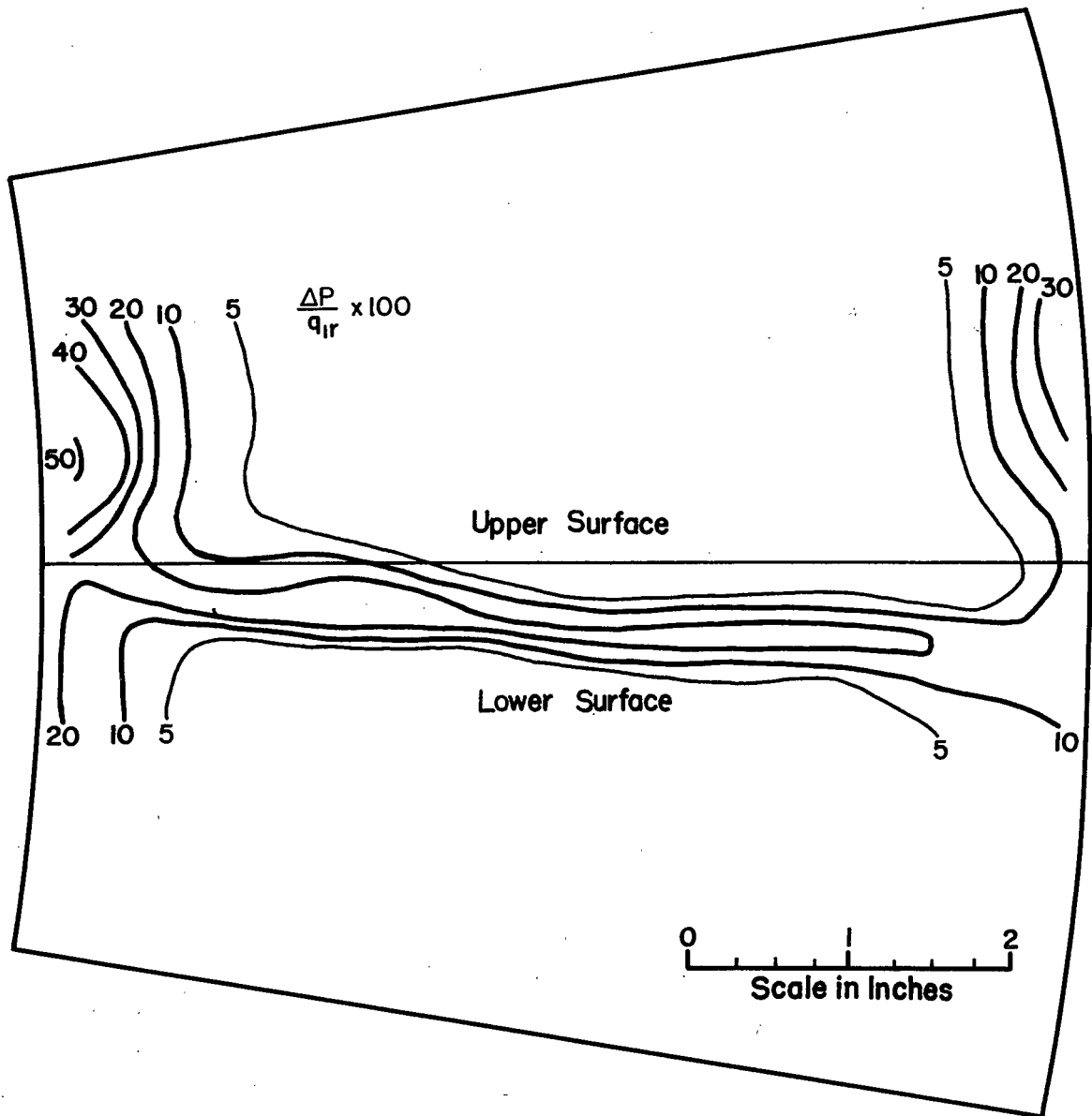
(a)  $\alpha_m = 8.5^\circ$ ;  $M_m = 0.361$ .

Figure 8.- Total-pressure-loss contours for the 1,000-hp compressor rotor (NACA 65-series compressor blade) at various angles of attack.



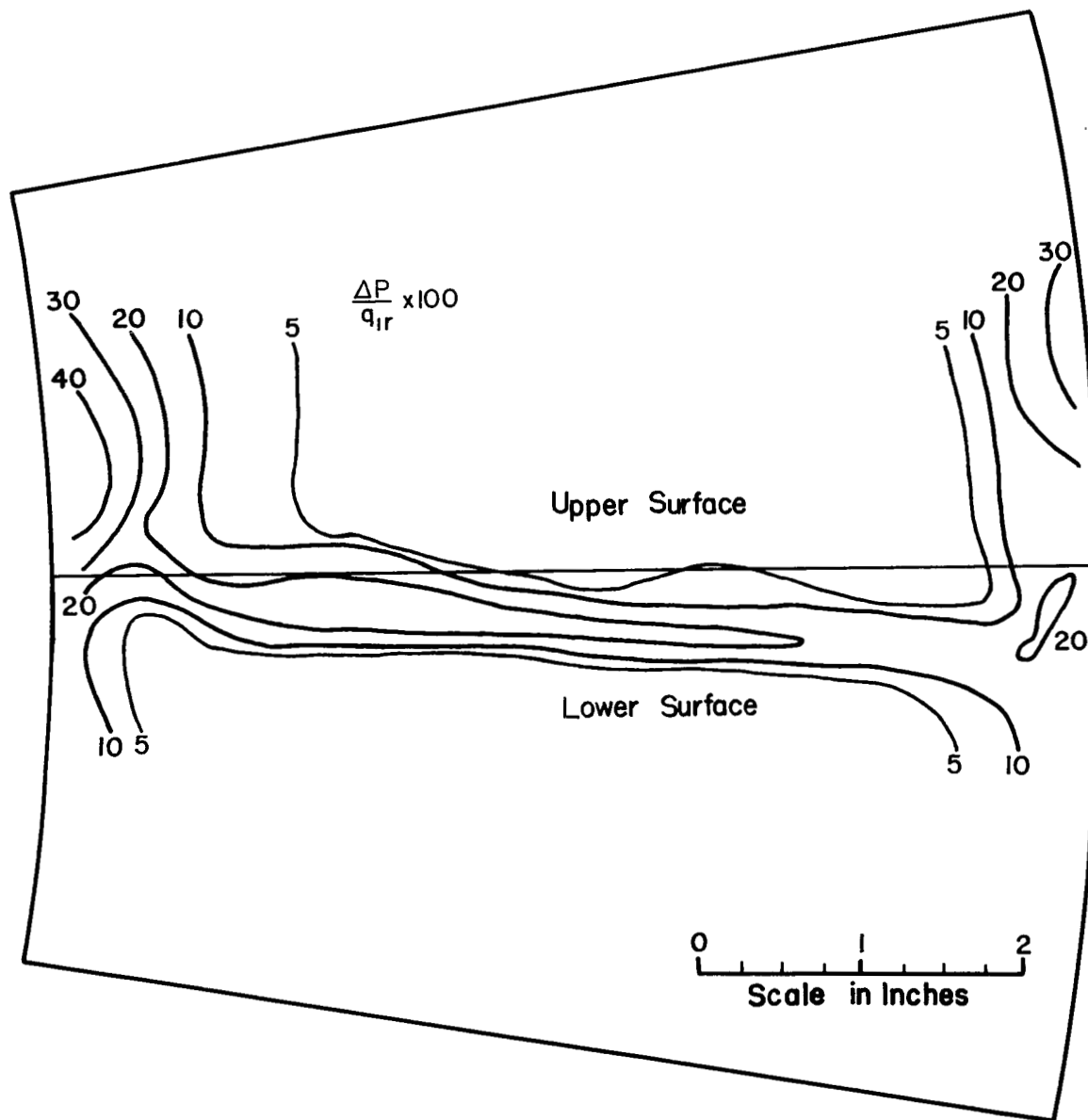
(b)  $\alpha_m = 9.3^\circ$ ;  $M_m = 0.337$ .

Figure 8.- Continued.



(c)  $\alpha_m = 10.2^\circ$ ;  $M_m = 0.316$ .

Figure 8.- Continued.

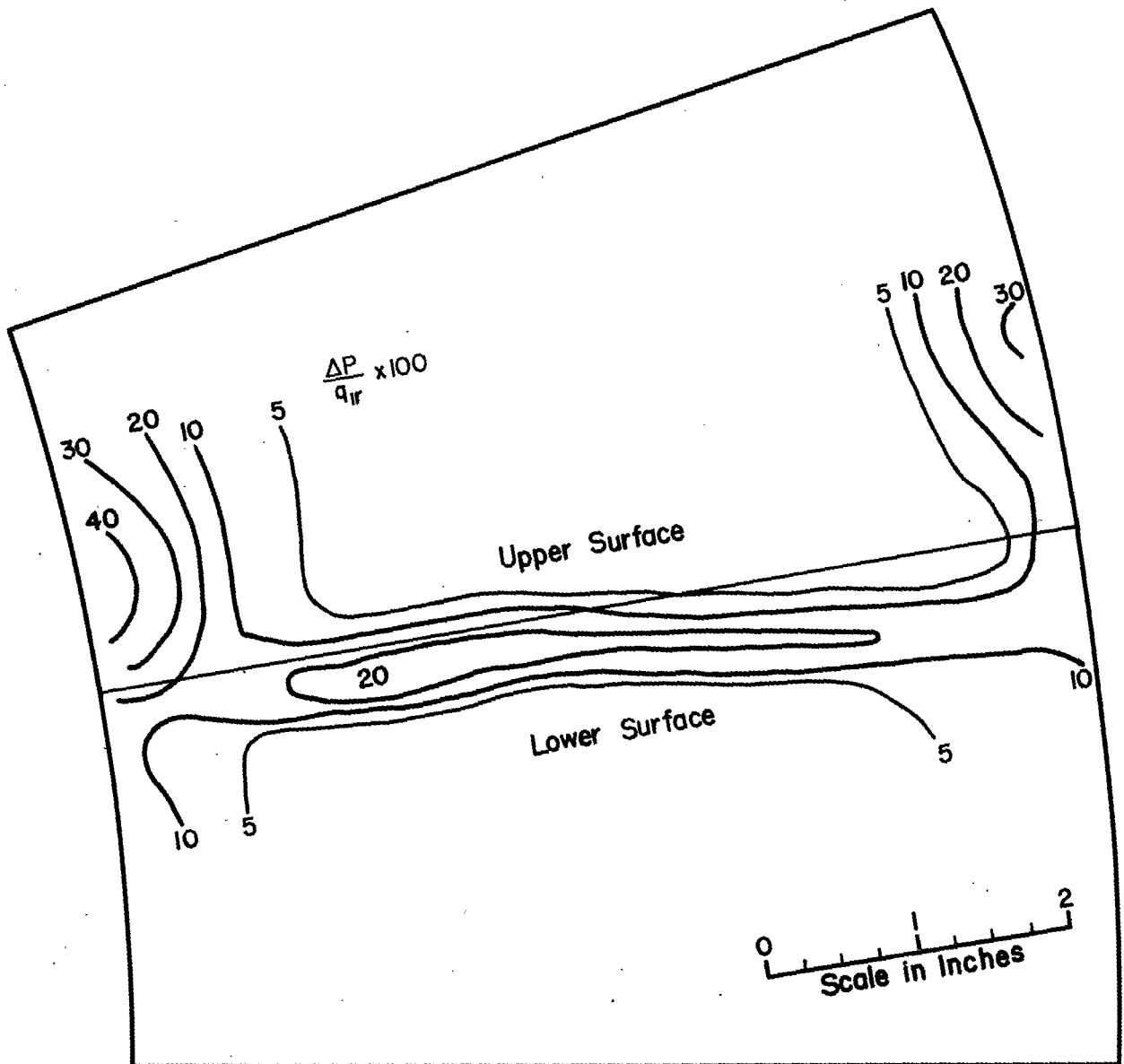


(d)  $\alpha_m = 12.4^\circ$ ;  $M_m = 0.277$ .

Figure 8.- Continued.

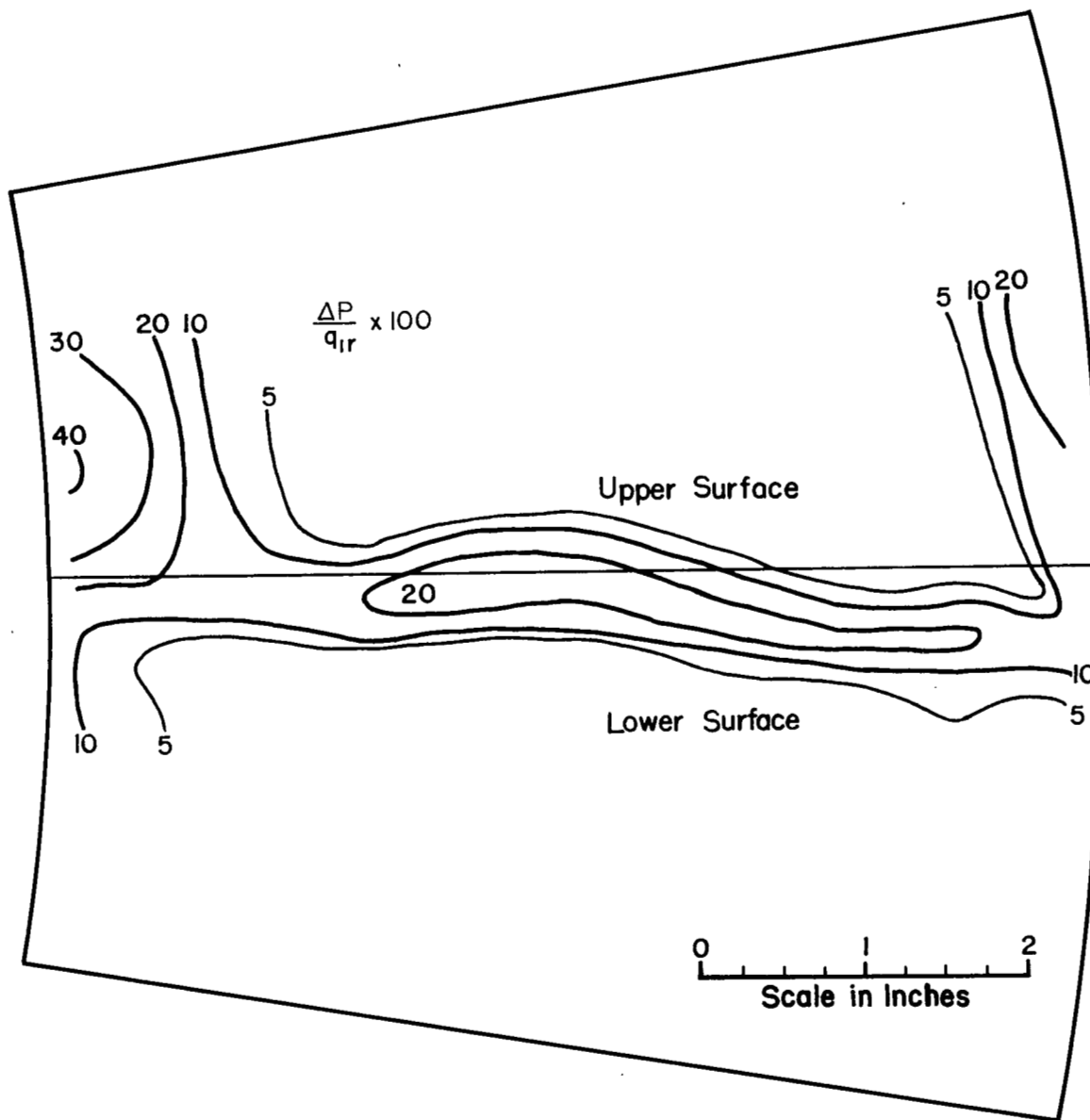


32



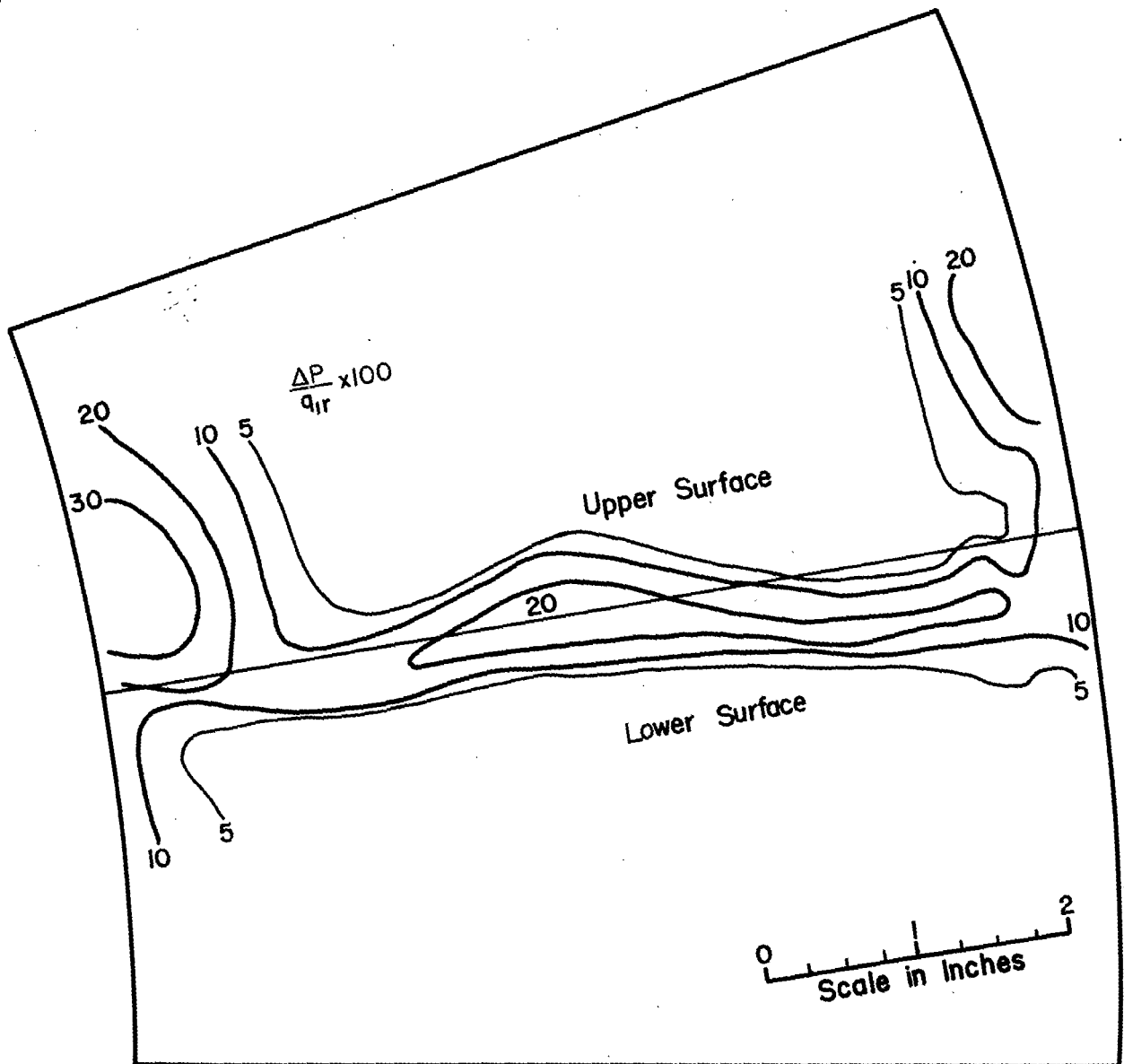
(e)  $\alpha_m = 13.5^\circ$ ;  $M_m = 0.258$ .

Figure 8.- Continued.



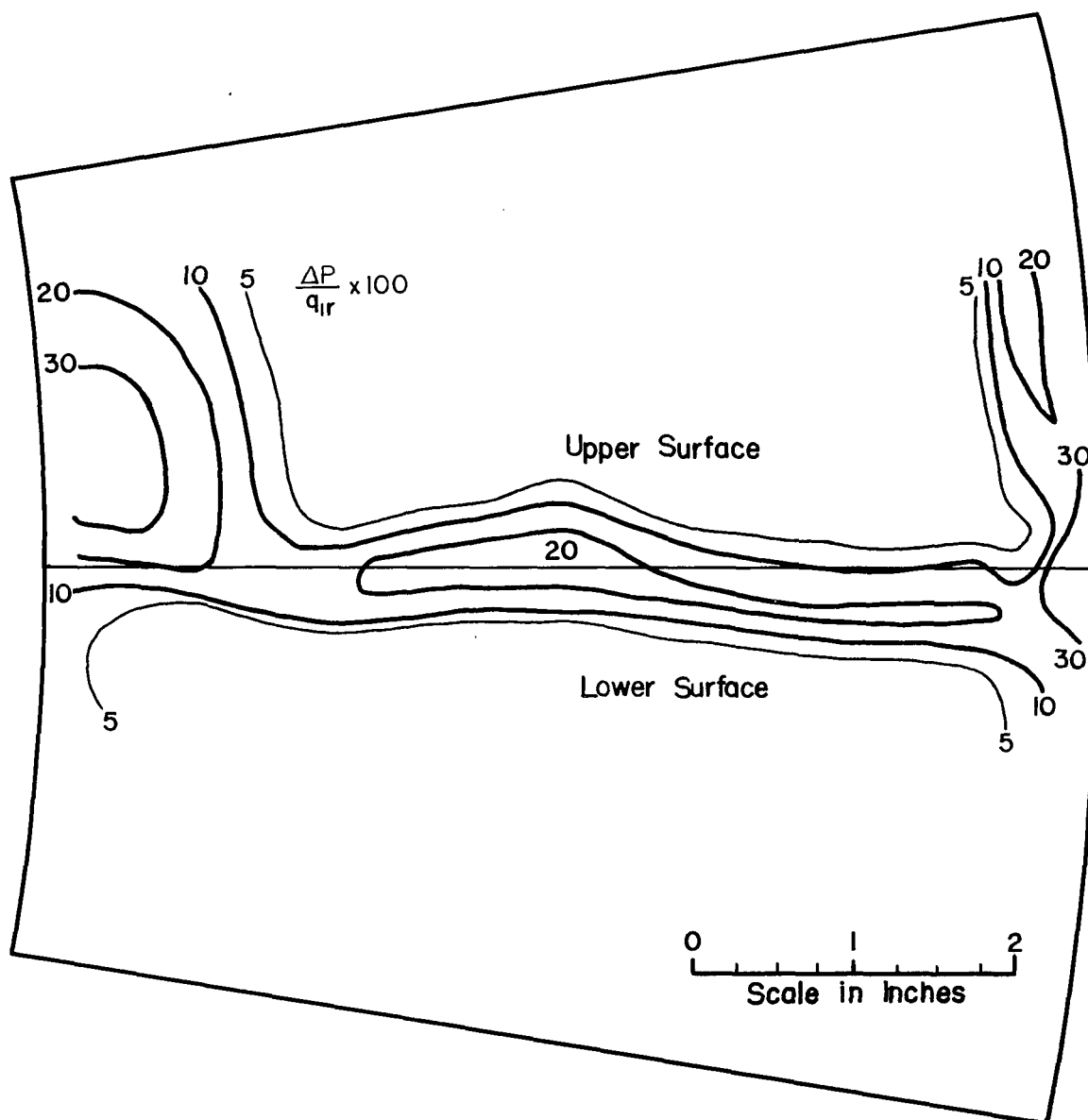
(f)  $\alpha_m = 15.4^\circ$ ;  $M_m = 0.237$ .

Figure 8.- Continued.



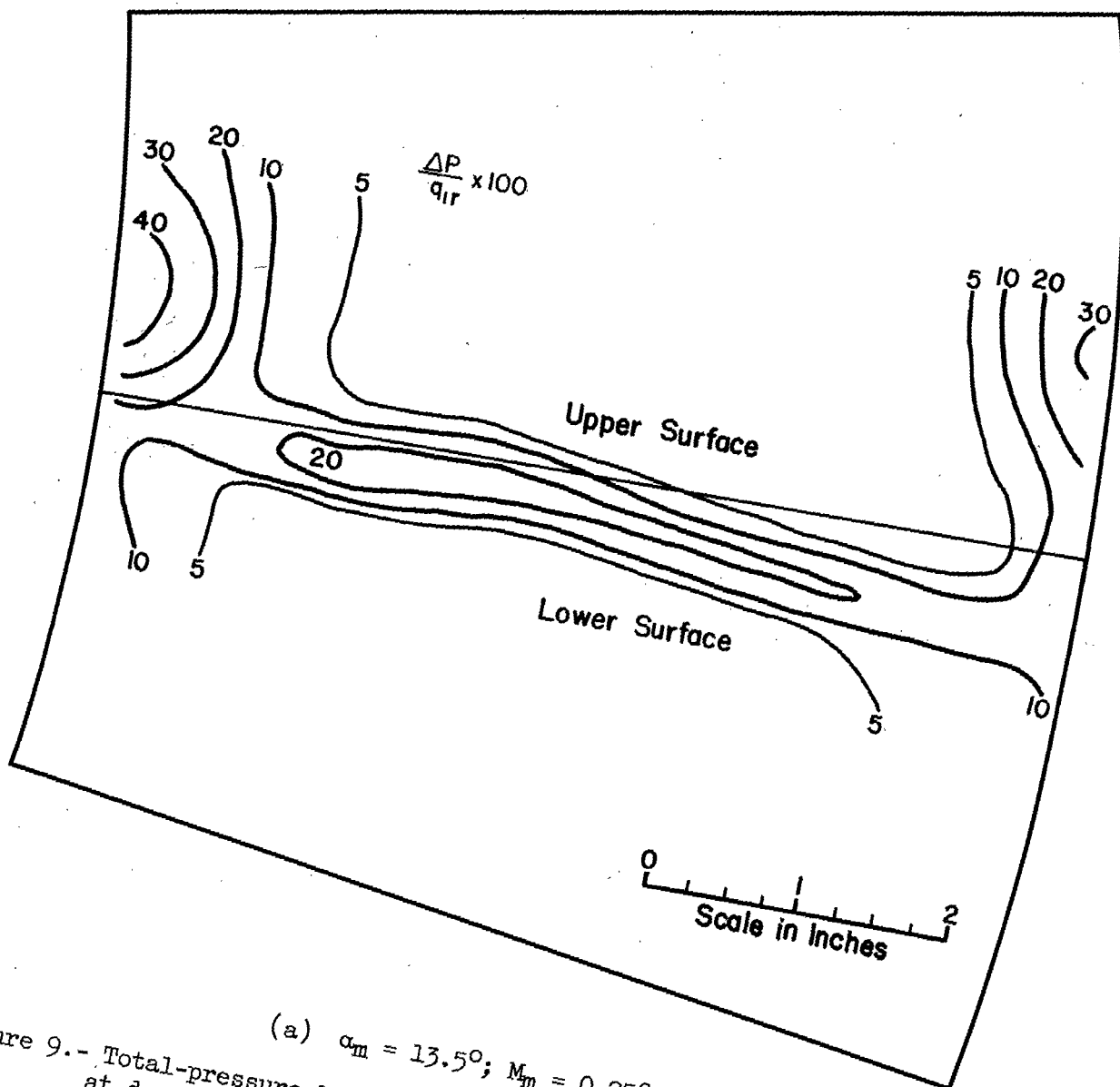
(g)  $\alpha_m = 16.8^\circ$ ;  $M_m = 0.221$ .

Figure 8.- Continued.



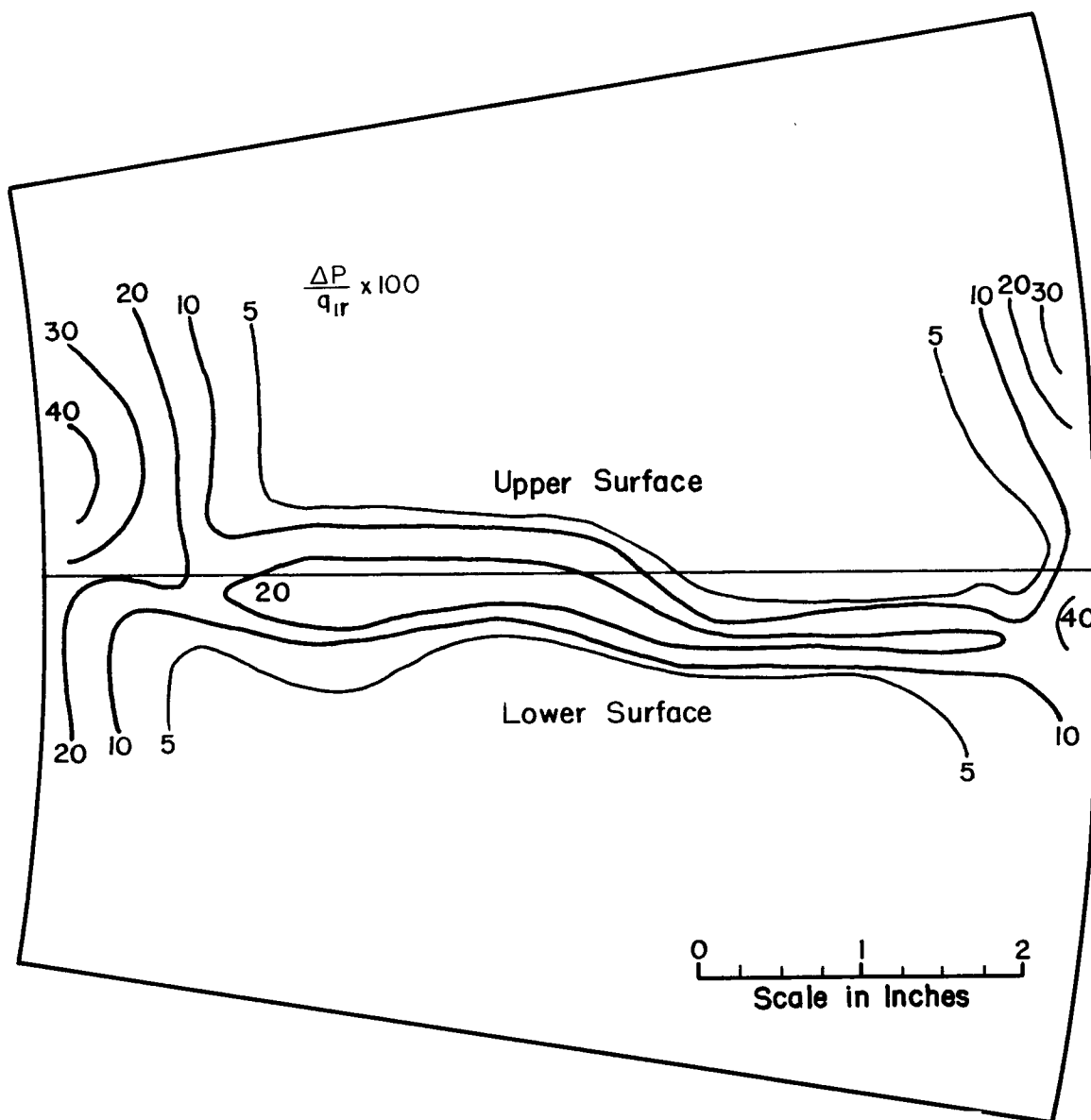
(h)  $\alpha_m = 17.5^\circ$ ;  $M_m = 0.215$ .

Figure 8.- Concluded.



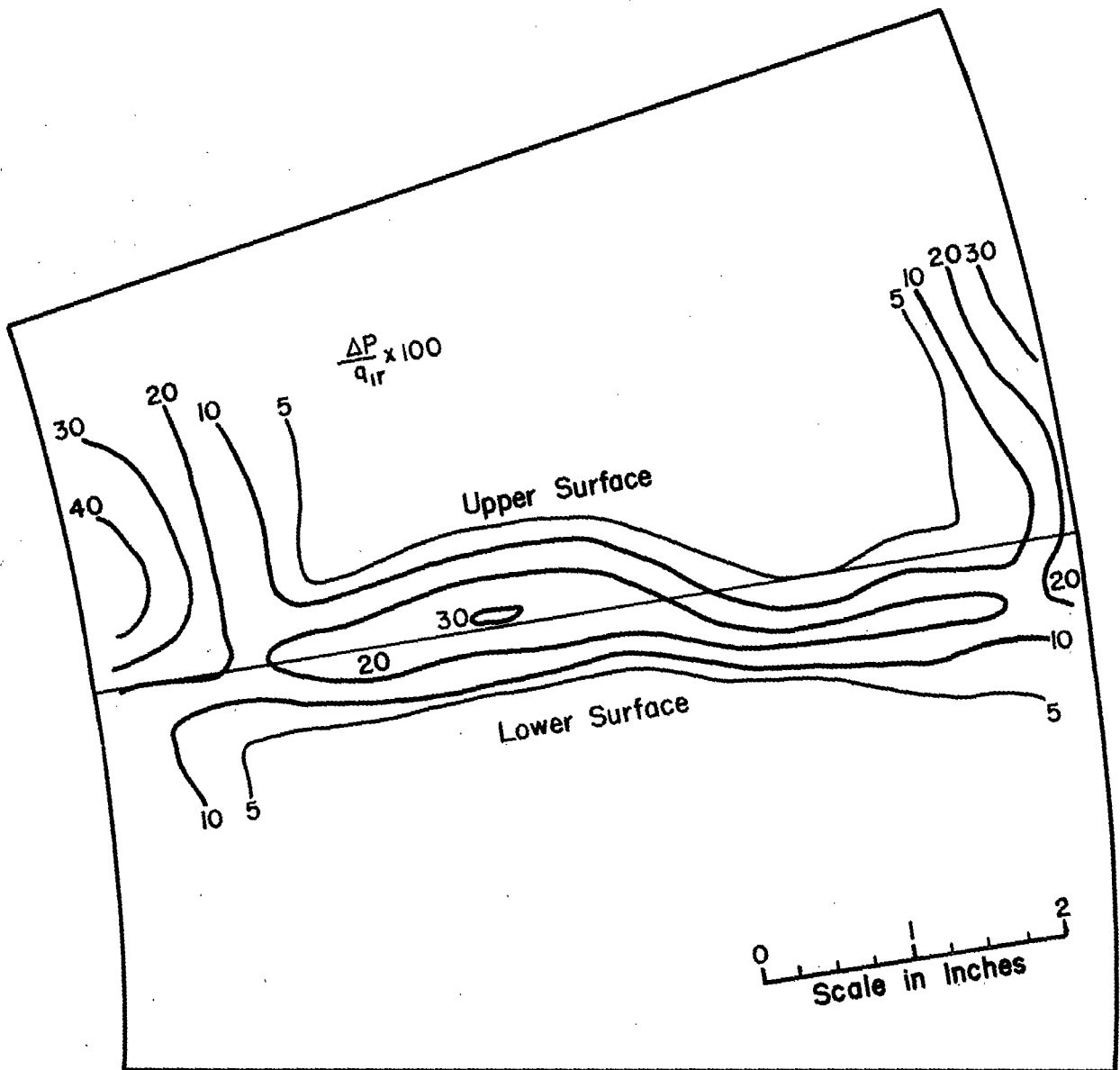
(a)  $\alpha_m = 13.5^\circ$ ;  $M_m = 0.258$ .

Figure 9.- Total-pressure-loss contours for the 1,000-hp compressor rotor at design angle of attack with Mach number variation.



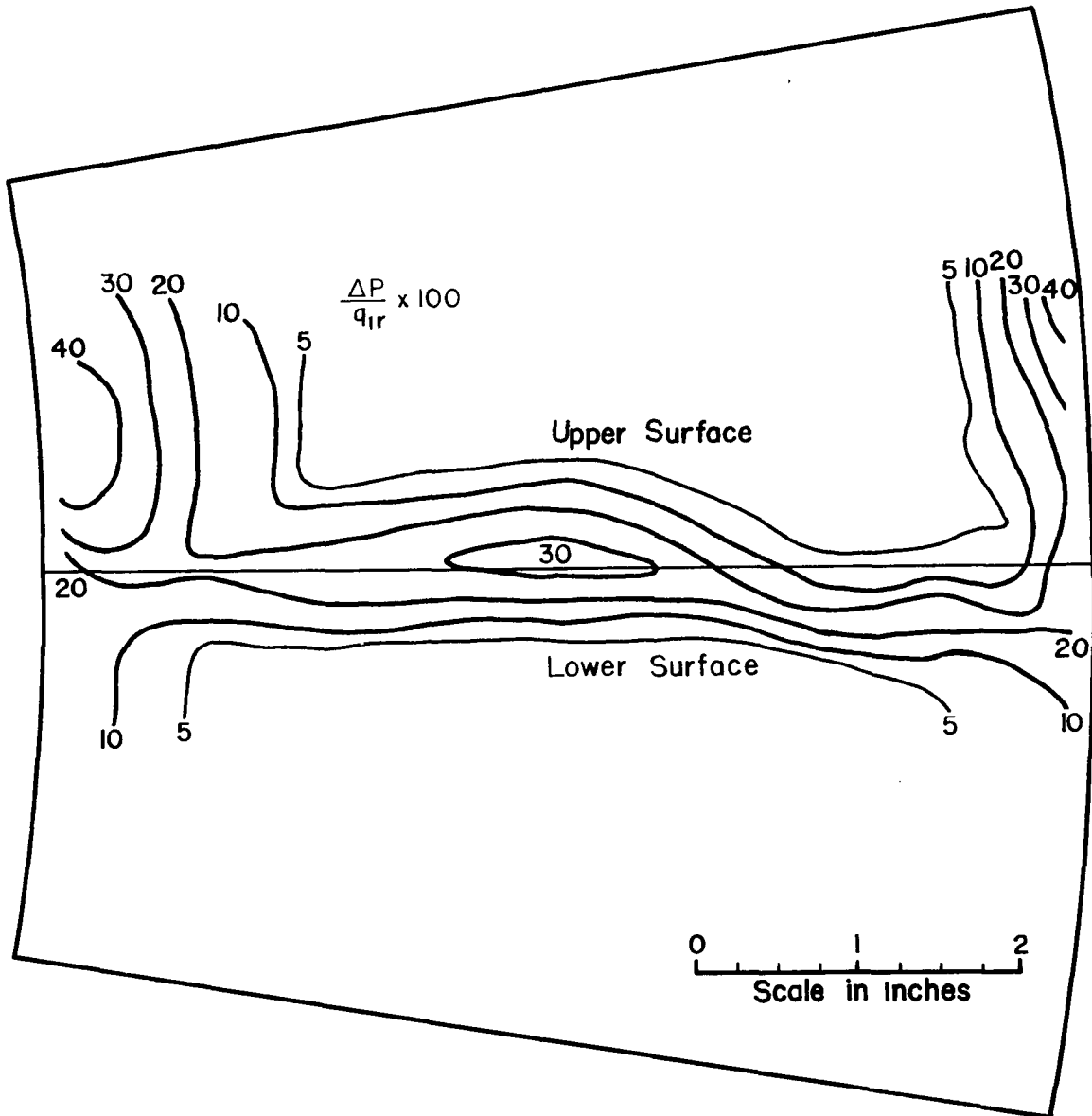
(b)  $\alpha_m = 13.8^\circ$ ;  $M_m = 0.367$ .

Figure 9.- Continued.



(c)  $\alpha_m = 14.1^\circ$ ;  $M_m = 0.517$ .

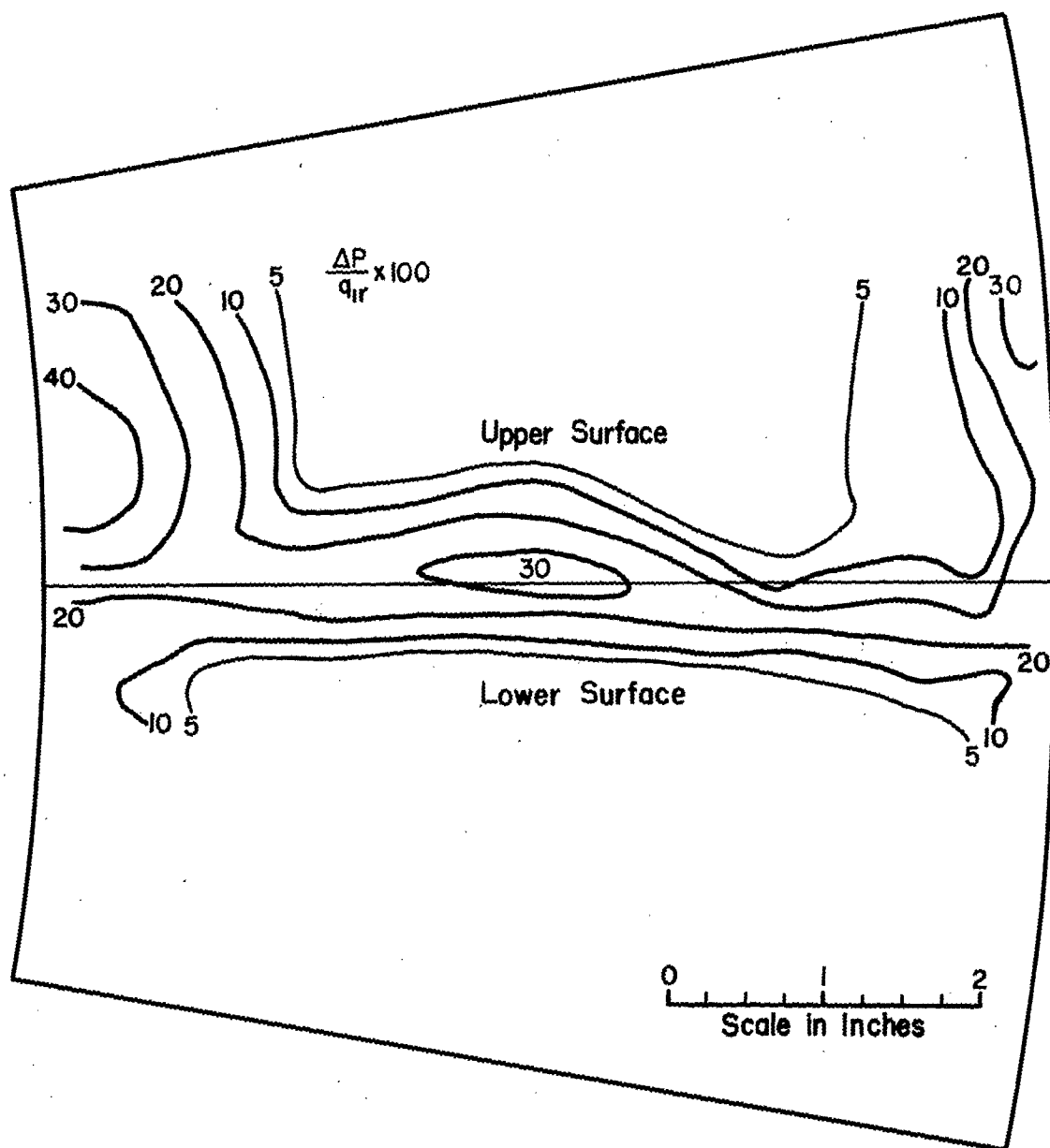
Figure 9.- Continued.



(d)  $\alpha_m = 14.3^\circ$ ;  $M_m = 0.610$ .

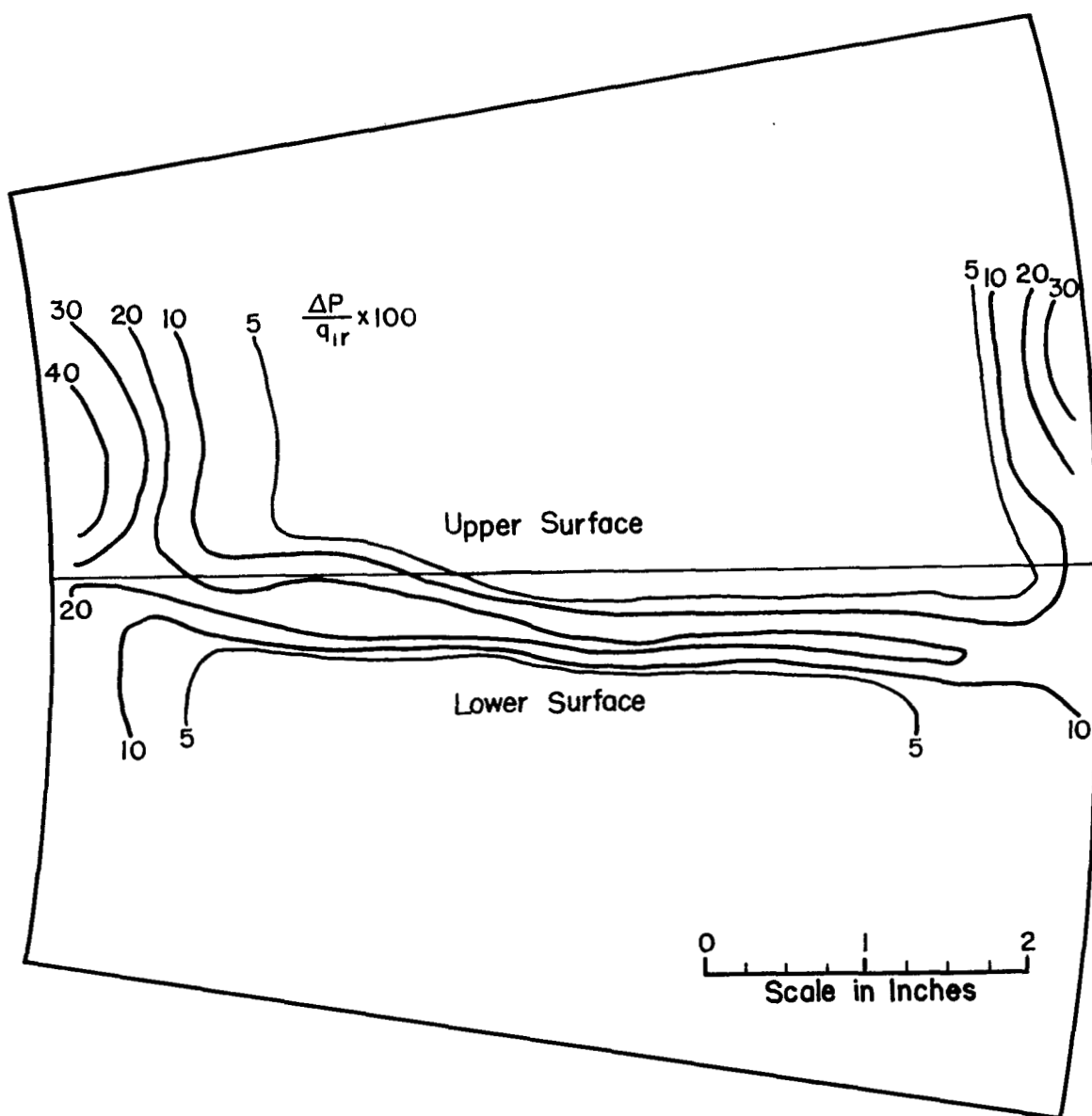
Figure 9.- Continued.





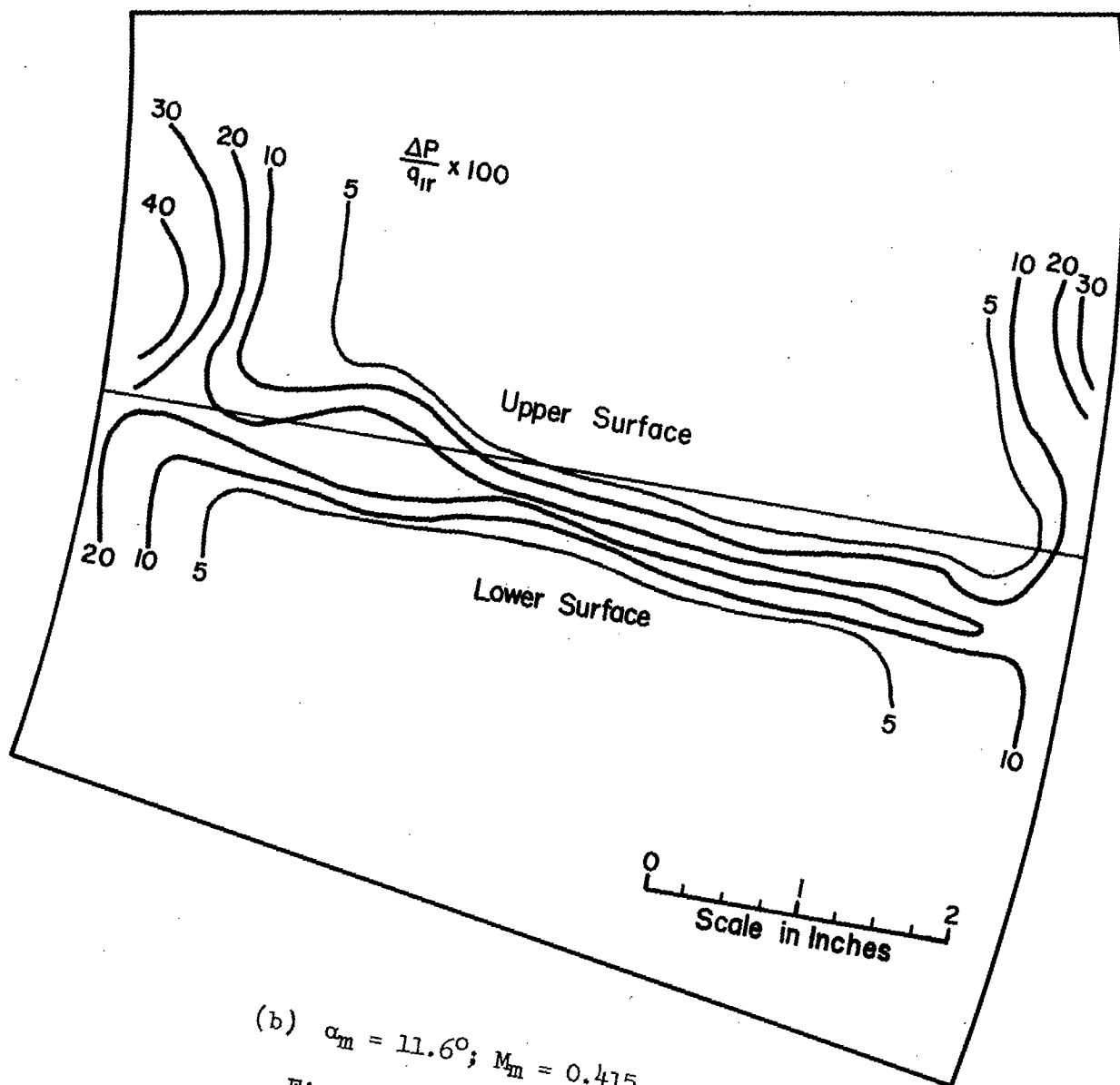
(e)  $\alpha_m = 14.3^\circ$ ;  $M_m = 0.676$ .

Figure 9.- Concluded.



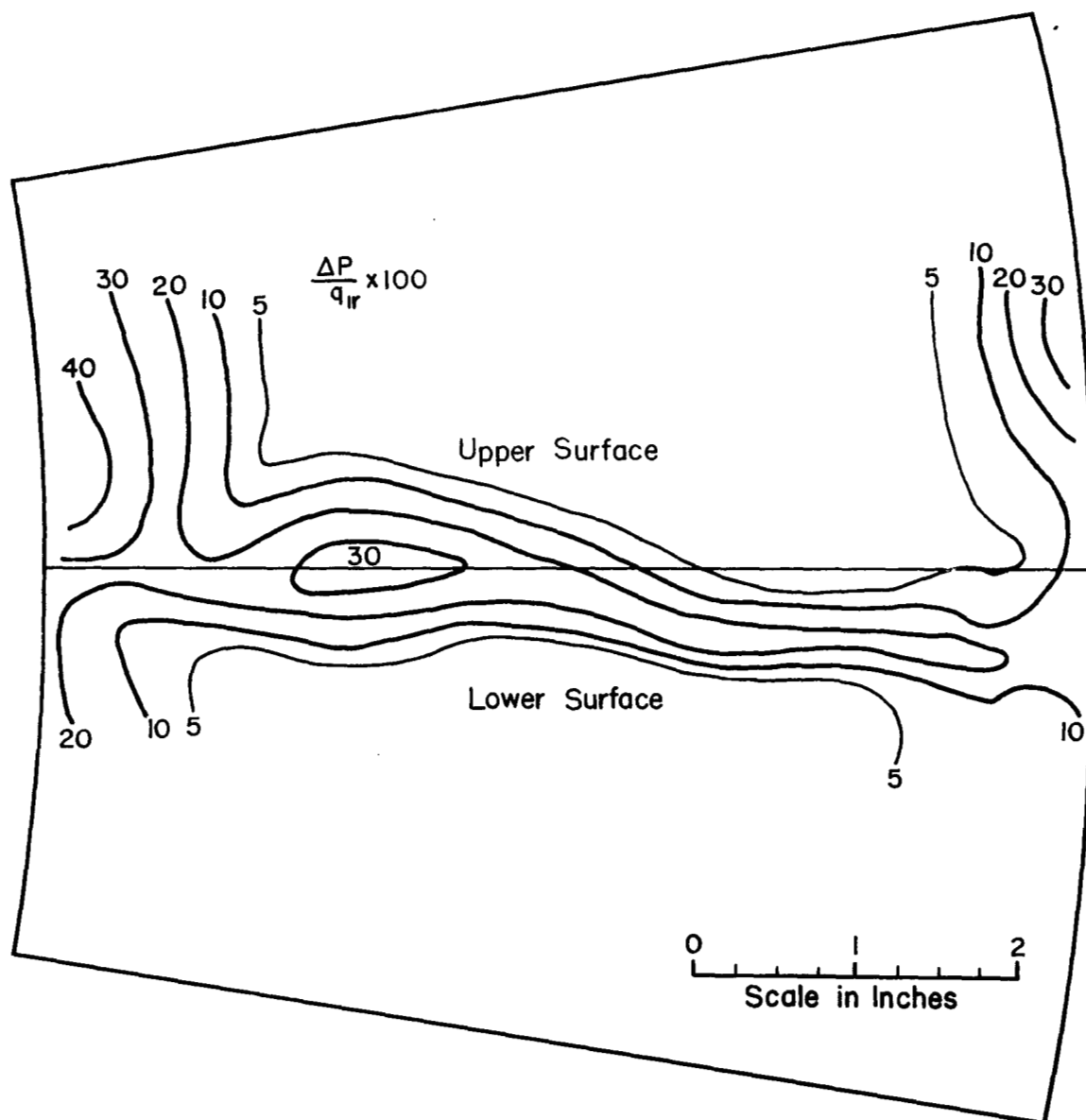
(a)  $\alpha_m = 11.2^\circ$ ;  $M_m = 0.295$ .

Figure 10.- Total-pressure-loss contours for the 1,000-hp compressor rotor at a below-design angle of attack with Mach number variation.



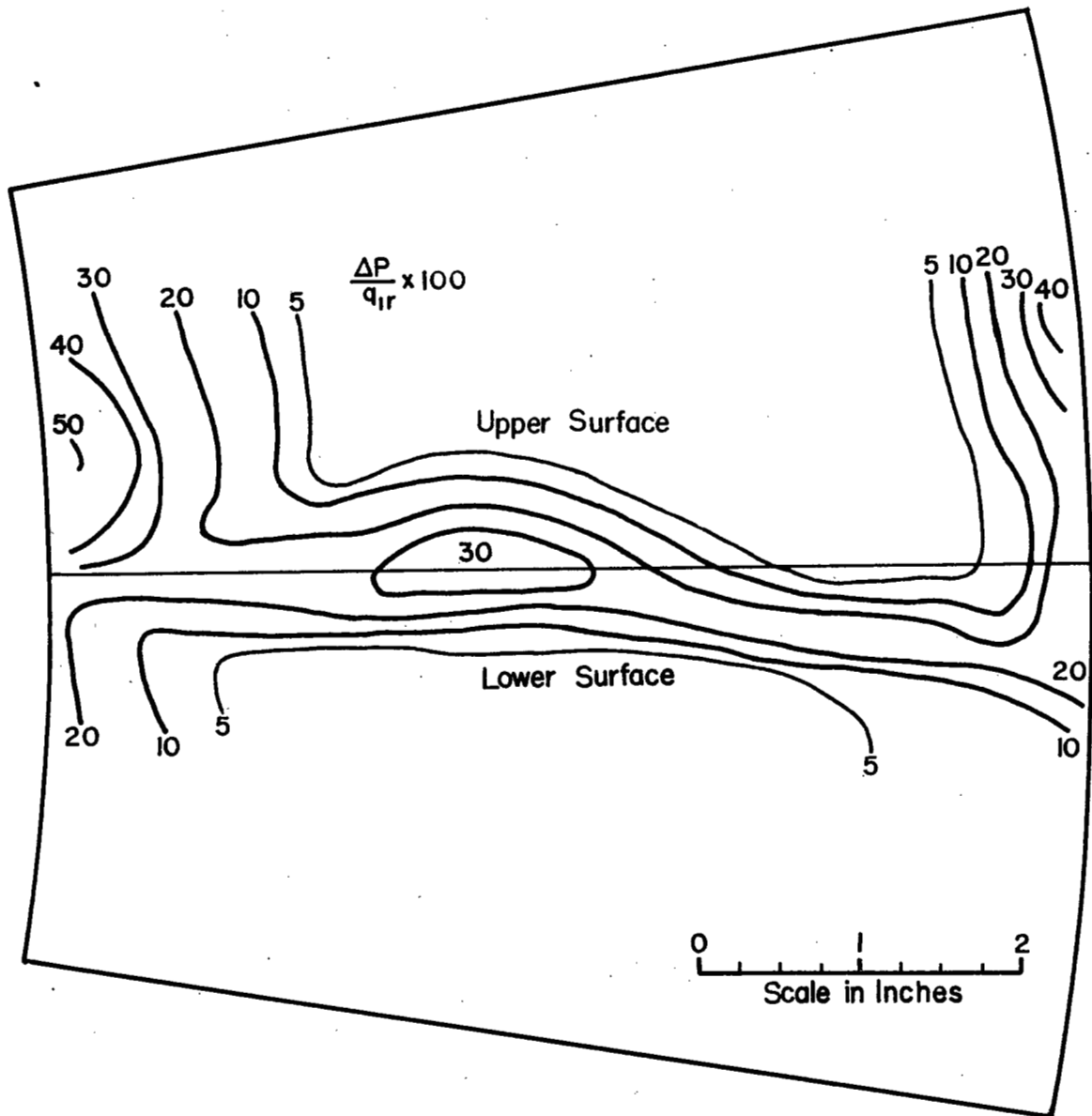
(b)  $\alpha_m = 11.6^\circ$ ;  $M_m = 0.415$ .

Figure 10.- Continued.



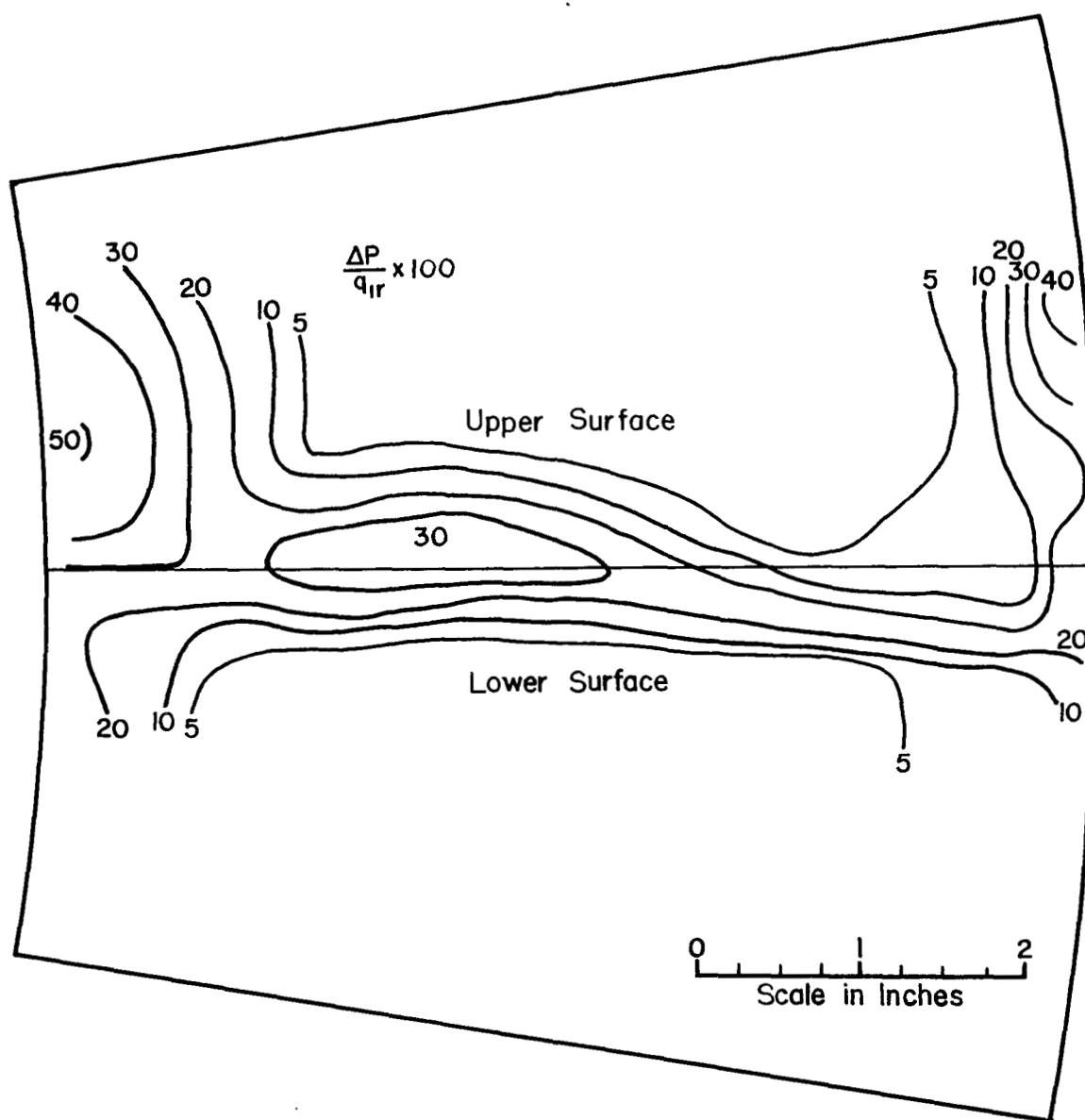
(c)  $\alpha_m = 12.0^\circ$ ;  $M_m = 0.582$ .

Figure 10.- Continued.



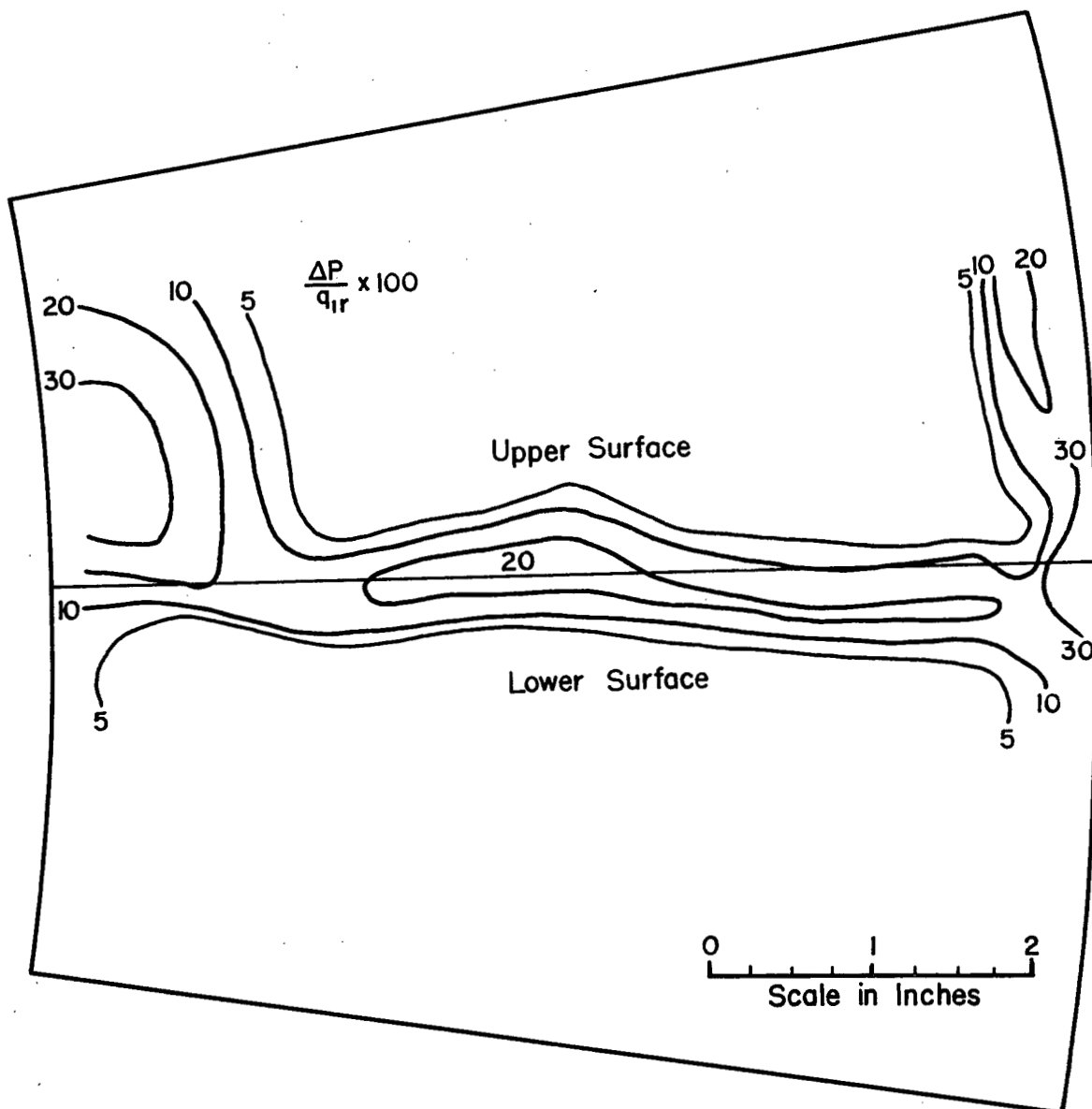
(d)  $\alpha_m = 11.9^\circ$ ;  $M_m = 0.705$ .

Figure 10.- Continued.



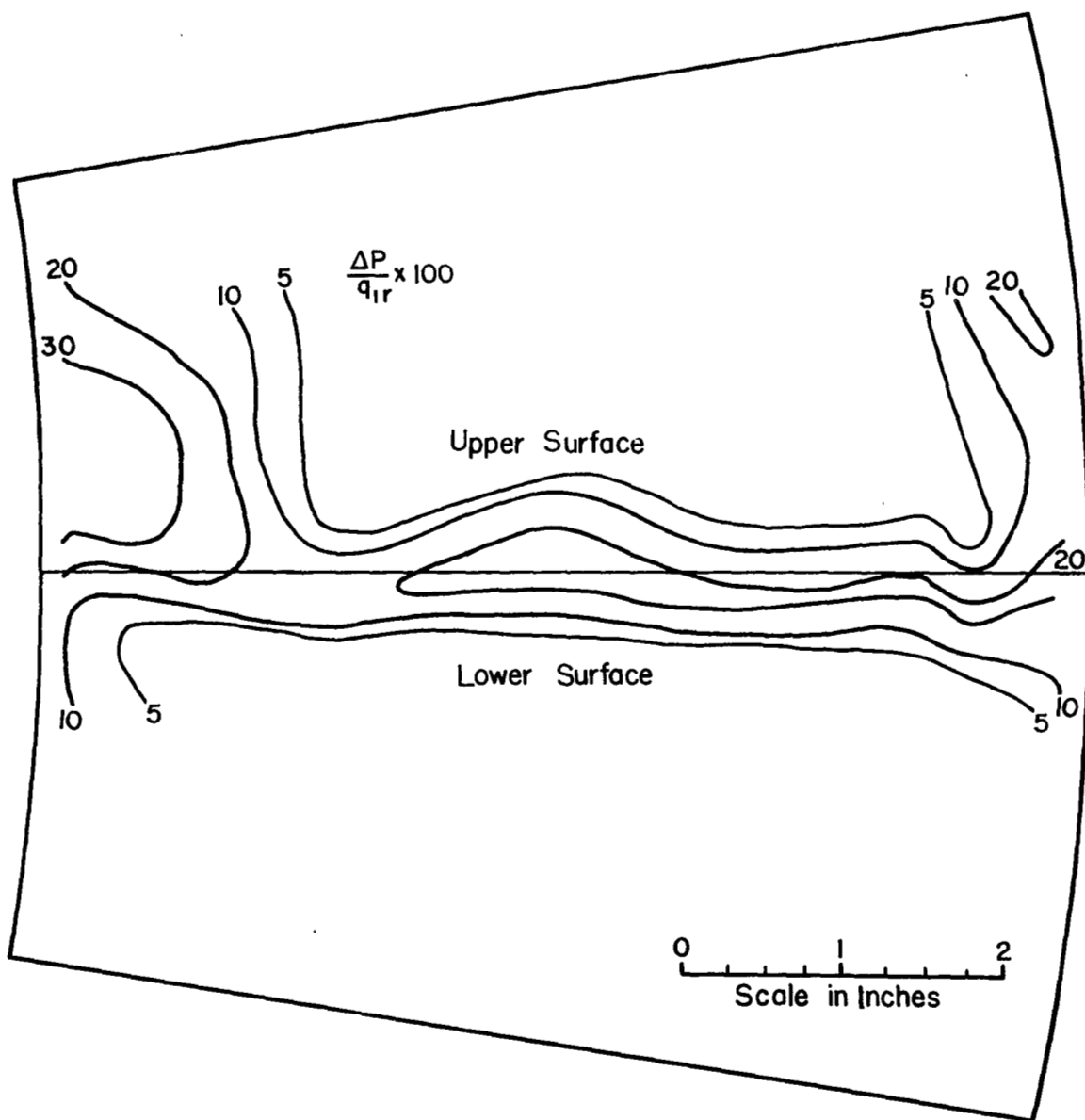
(e)  $\alpha_m = 11.4^\circ$ ;  $M_m = 0.809$ .

Figure 10.- Concluded.



(a)  $\alpha_m = 17.5^\circ$ ;  $M_m = 0.215$ .

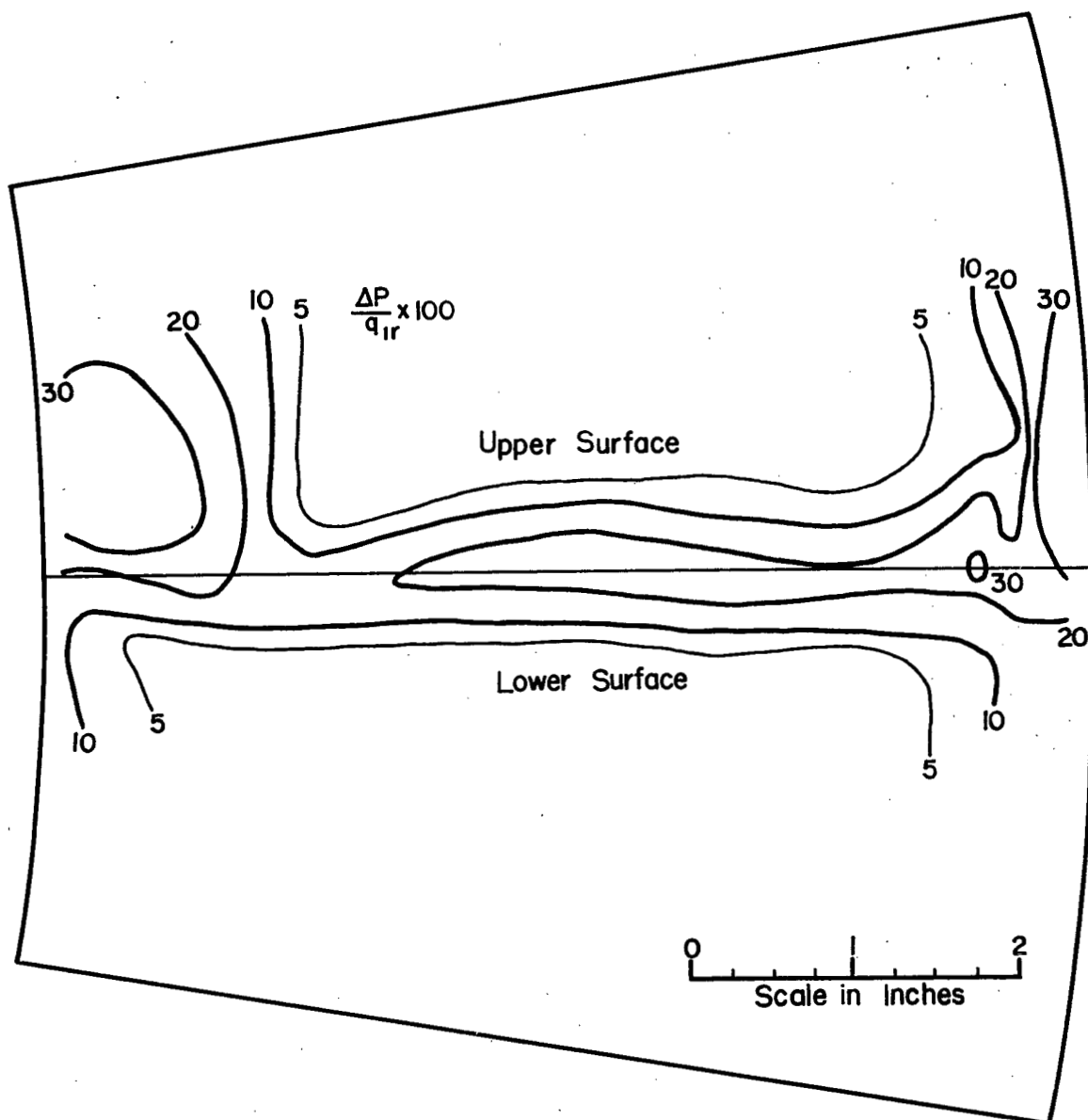
Figure 11.- Total-pressure-loss contours for the 1,000-hp compressor rotor at a near-surge angle of attack with Mach number variation.



(b)  $\alpha_m = 17.8^\circ$ ;  $M_m = 0.303$ .

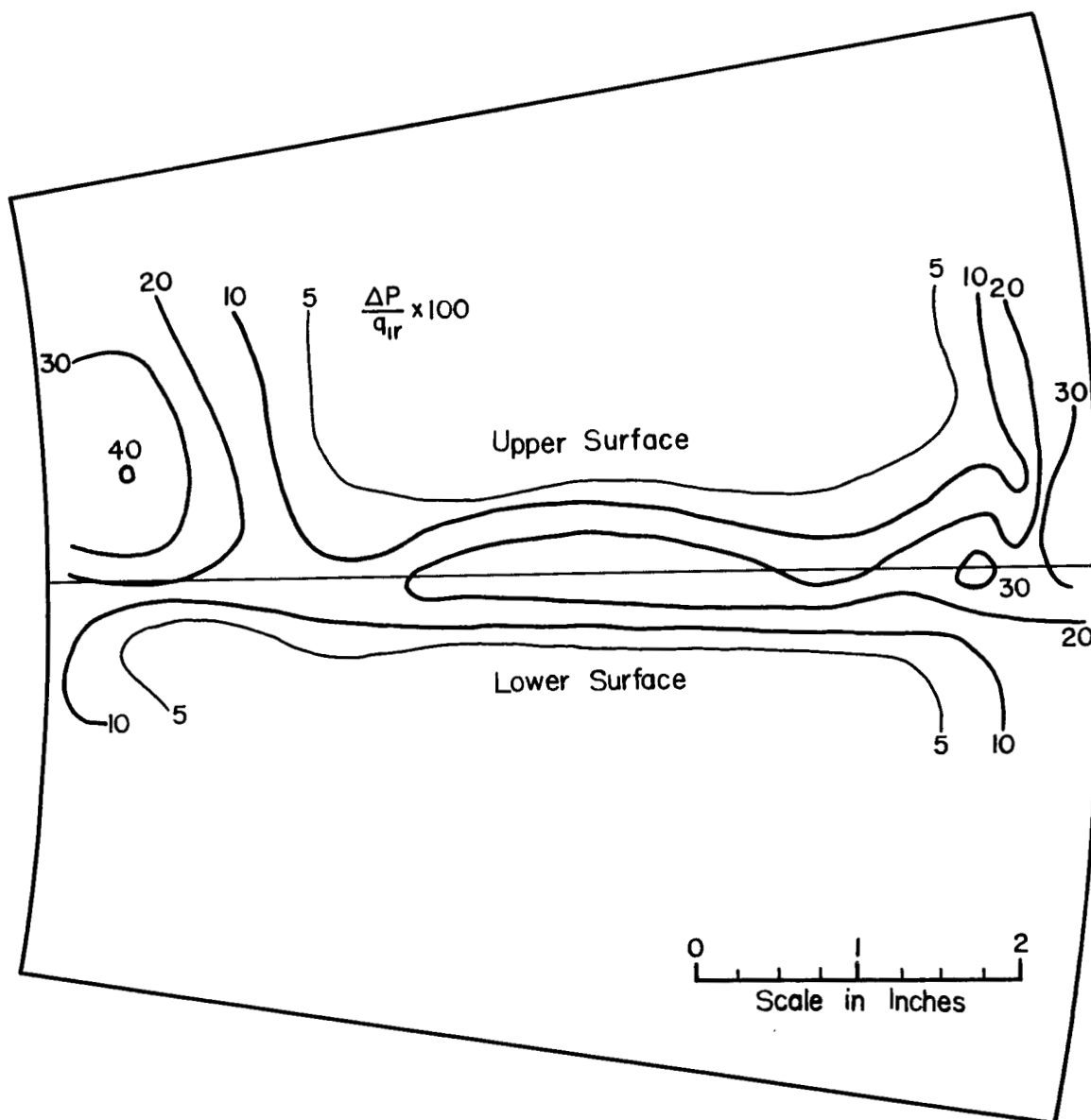
Figure 11.- Continued.





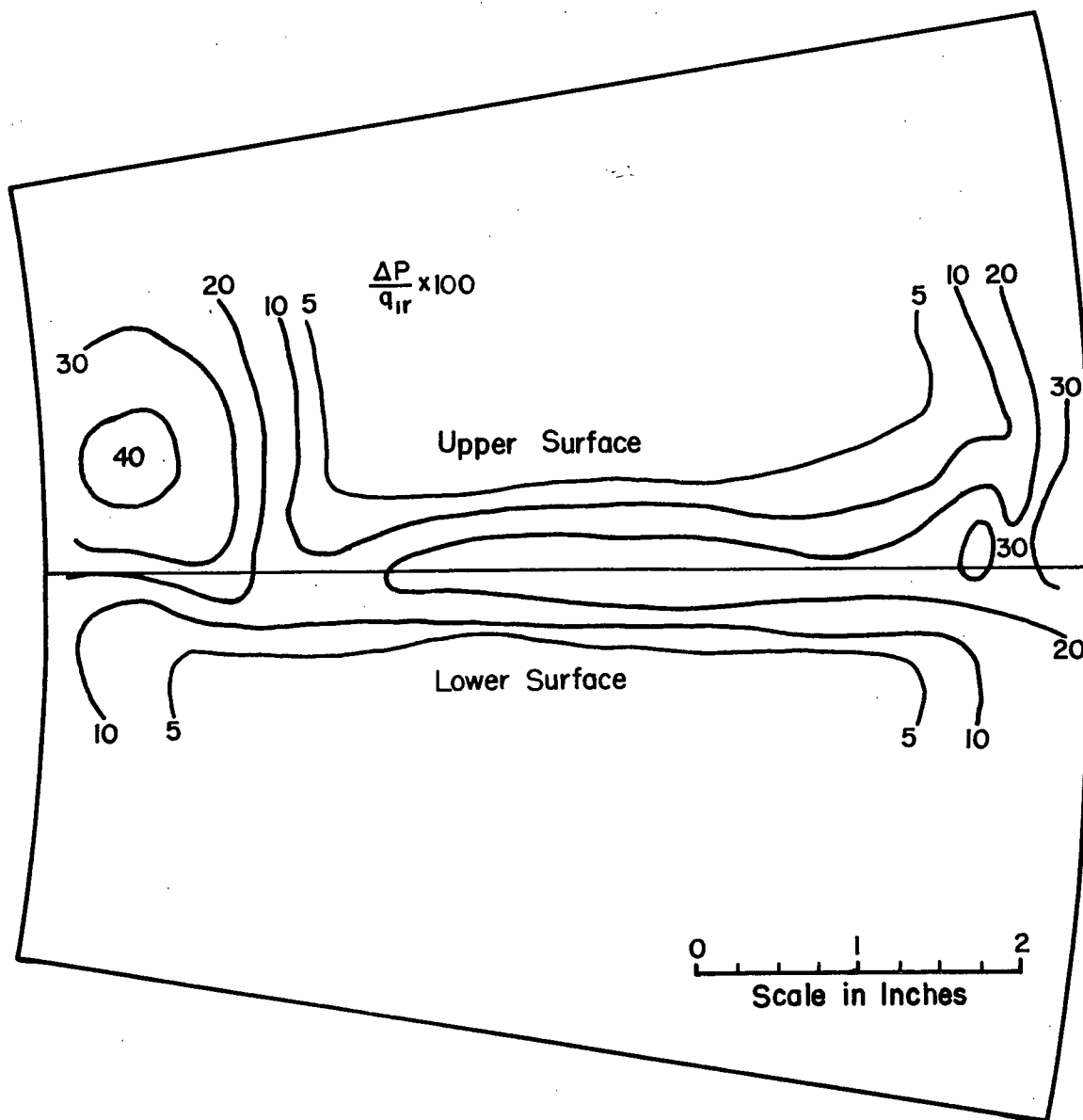
(c)  $\alpha_m = 18.0^\circ$ ;  $M_m = 0.428$ .

Figure 11.- Continued.



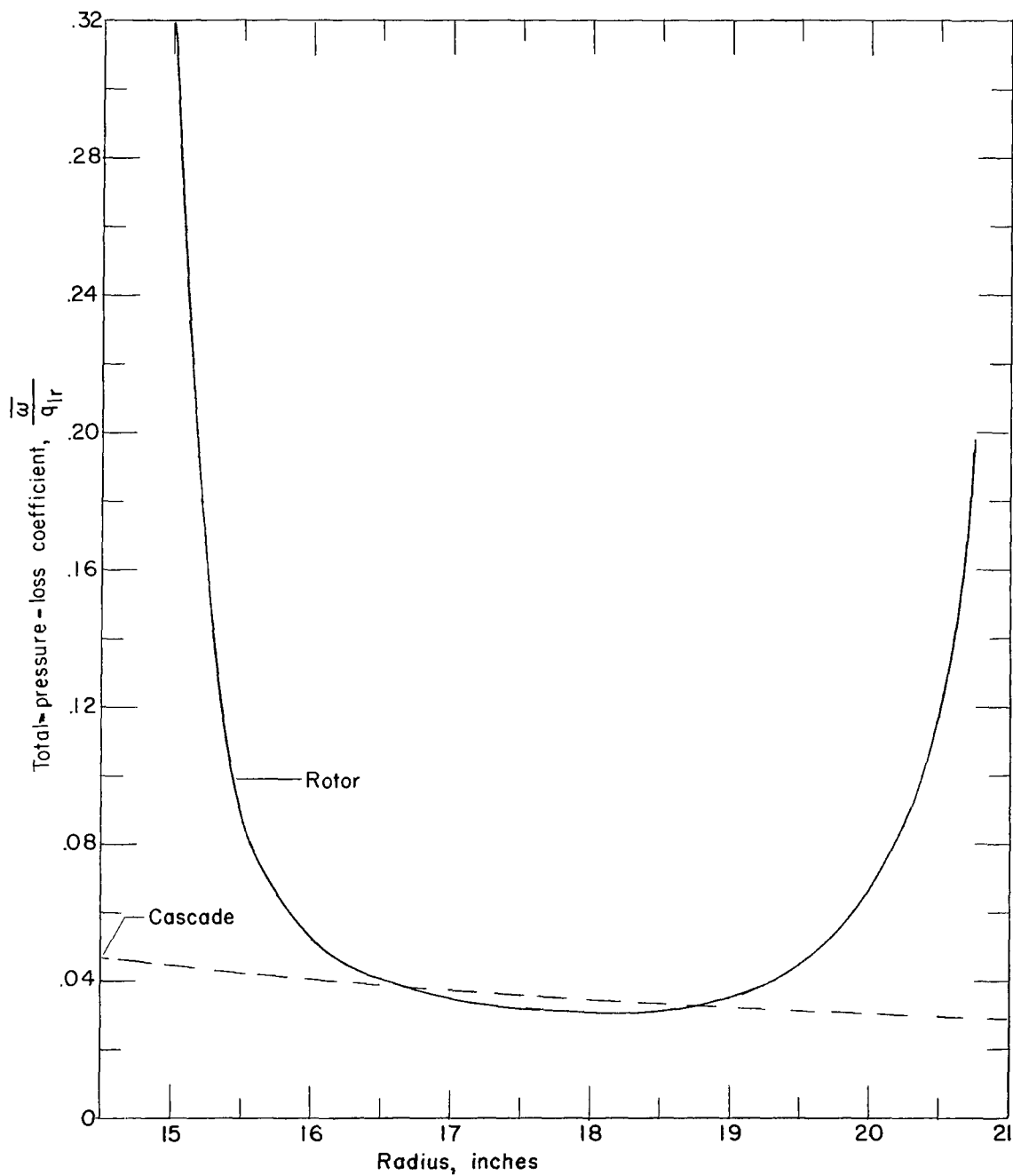
(d)  $\alpha_m = 17.5^\circ$ ;  $M_m = 0.522$ .

Figure 11.- Continued.



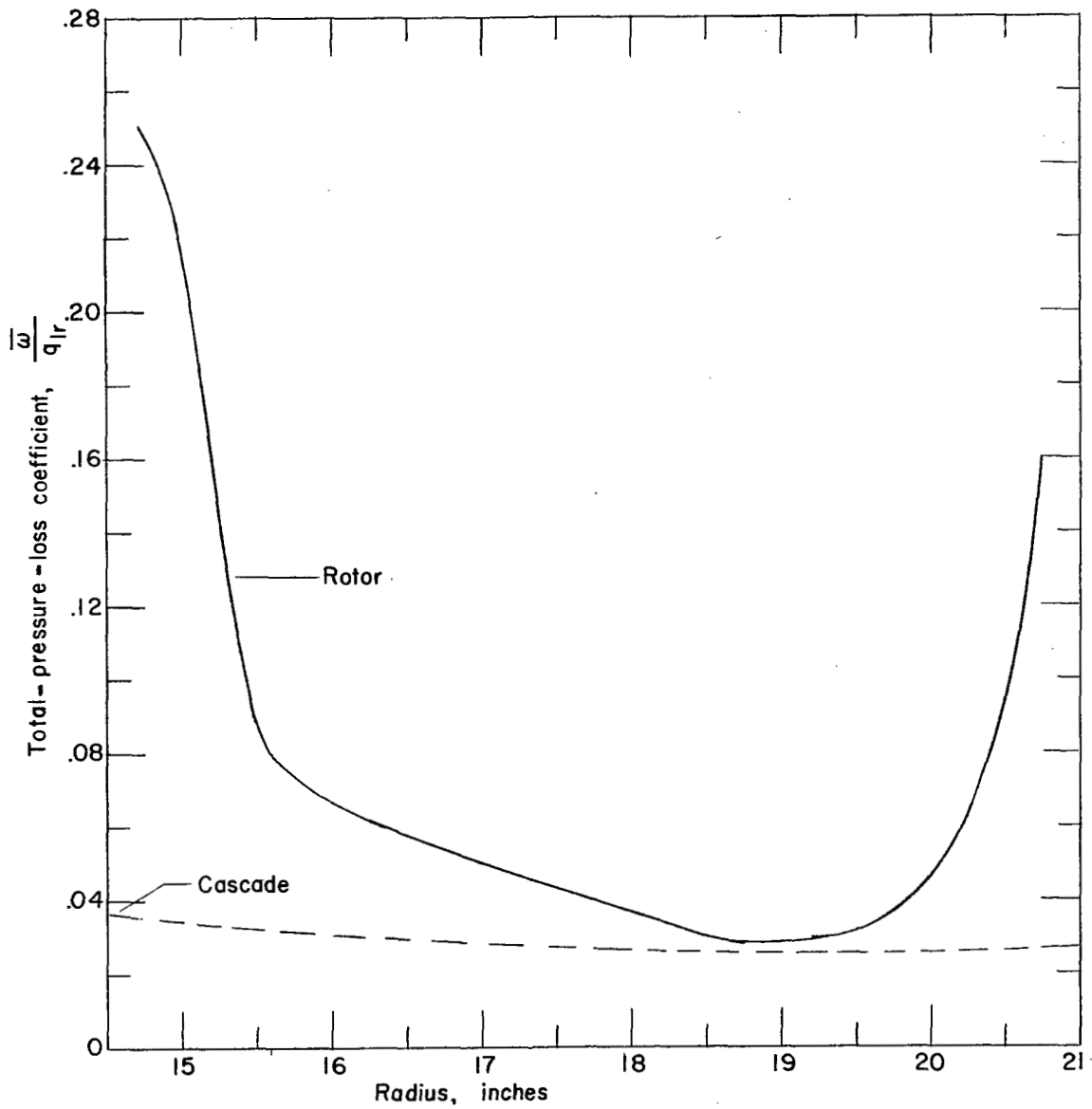
(e)  $\alpha_m = 17.4^\circ$ ;  $M_m = 0.580$ .

Figure 11.- Concluded.



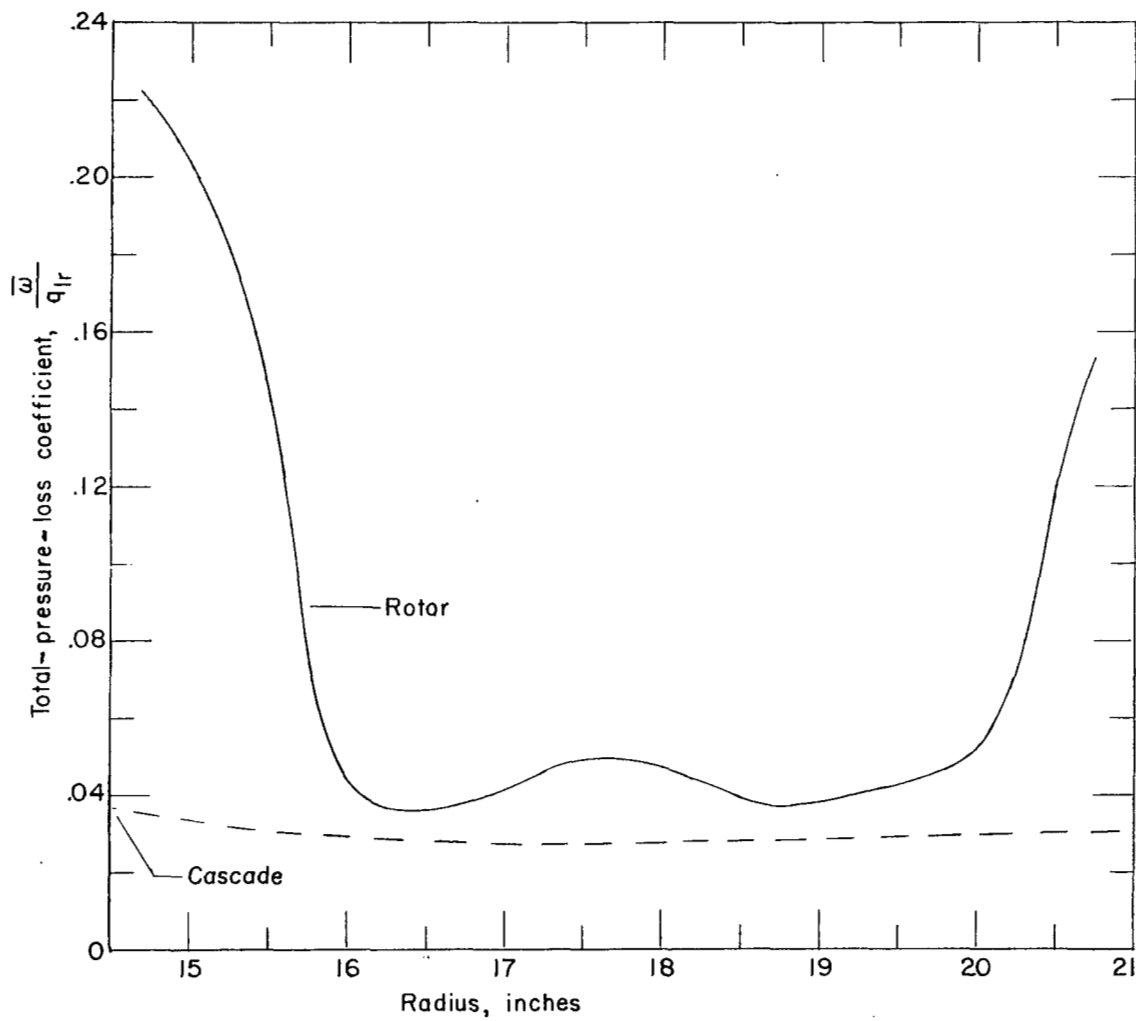
(a)  $\alpha_m = 8.8^\circ$ ;  $M_m = 0.507$ .

Figure 12.- Comparison of blower and cascade loss coefficients with radial position.



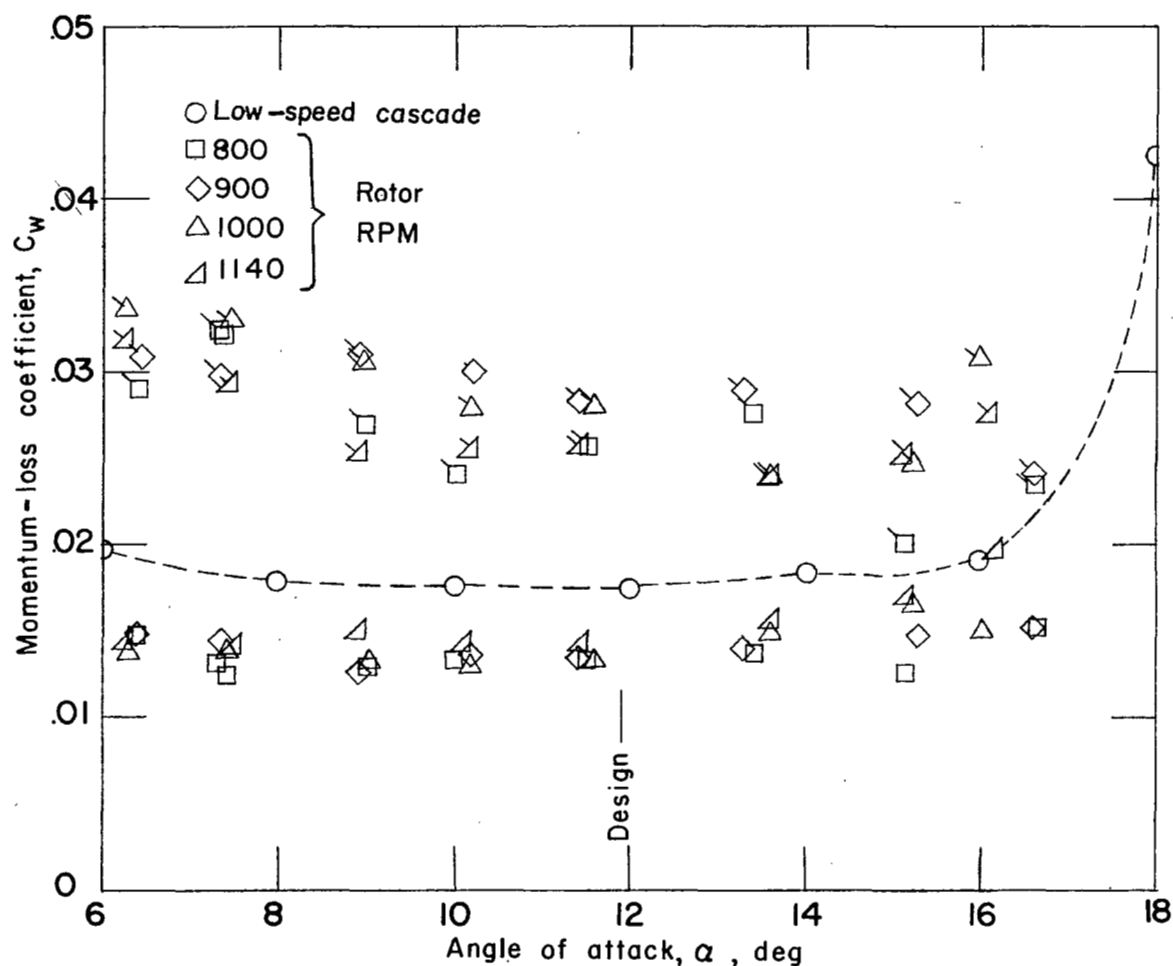
(b)  $\alpha_m = 13.8^\circ$ ;  $M_m = 0.367$ .

Figure 12.- Continued.



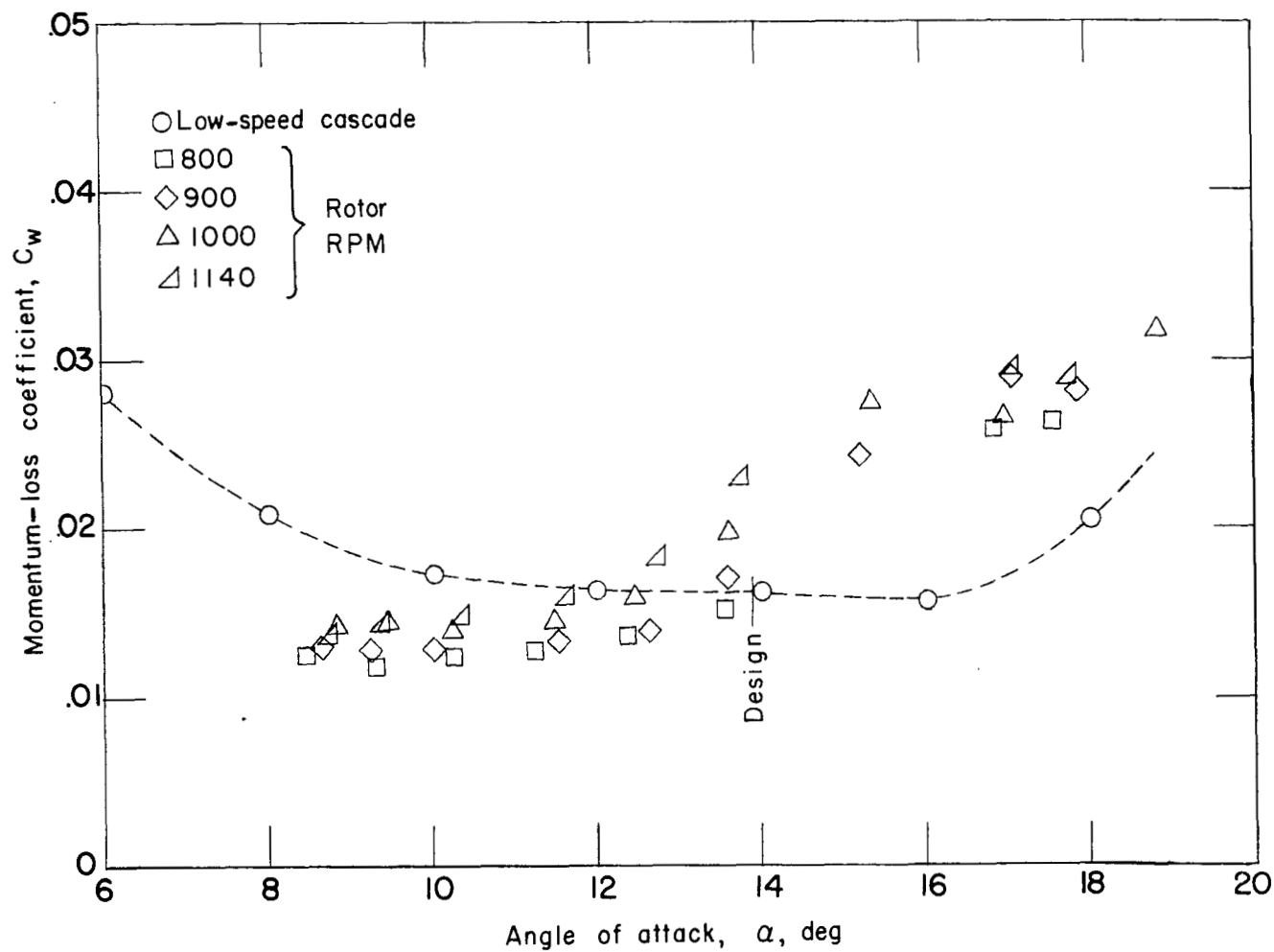
(c)  $\alpha_m = 17.8^\circ$ ;  $M_m = 0.303$ .

Figure 12.- Concluded.



(a) Outboard section.

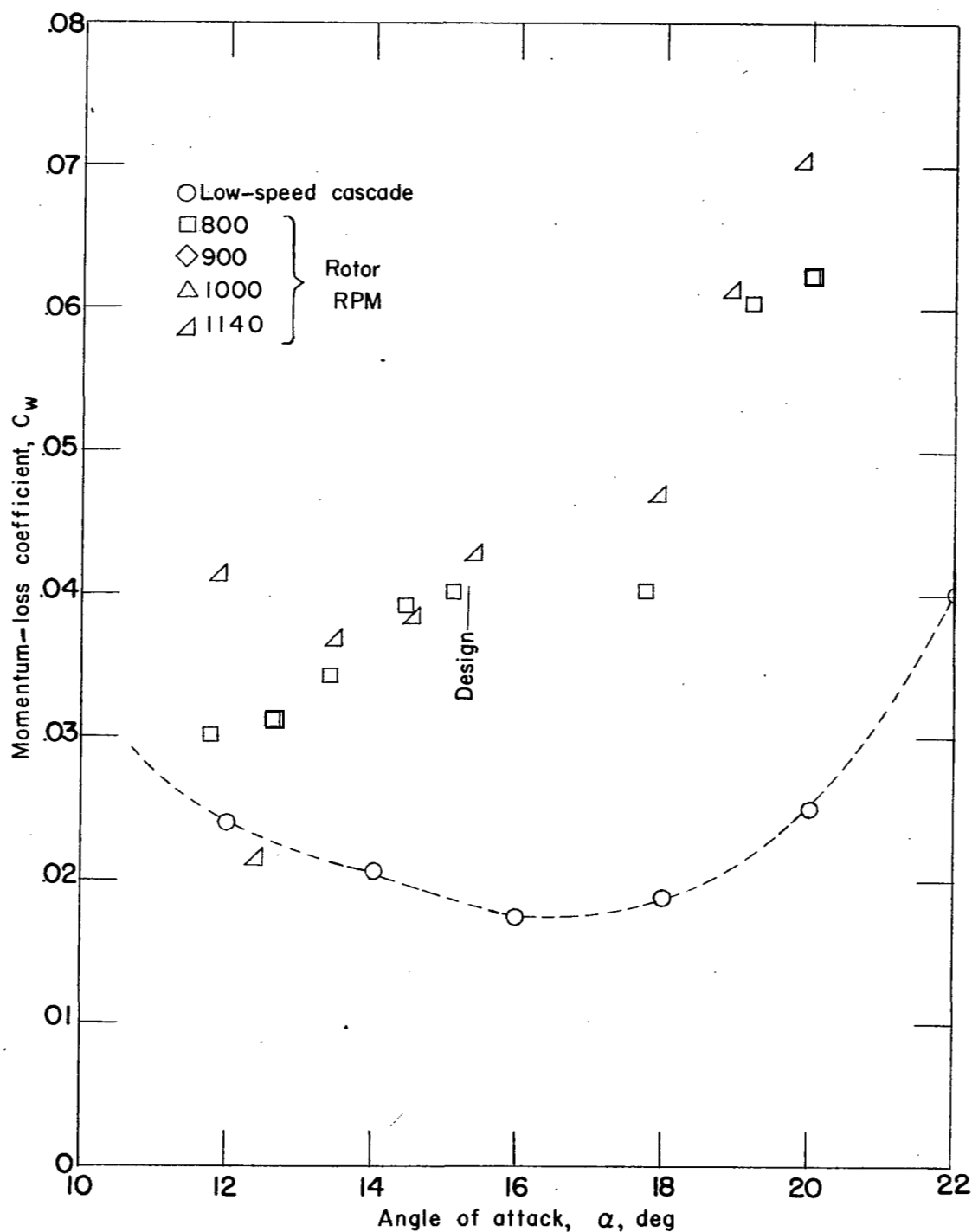
Figure 13.- Low-speed momentum-loss coefficient against angle of attack.  
Flagged symbols include casing boundary-layer loss.



(b) Mean section.

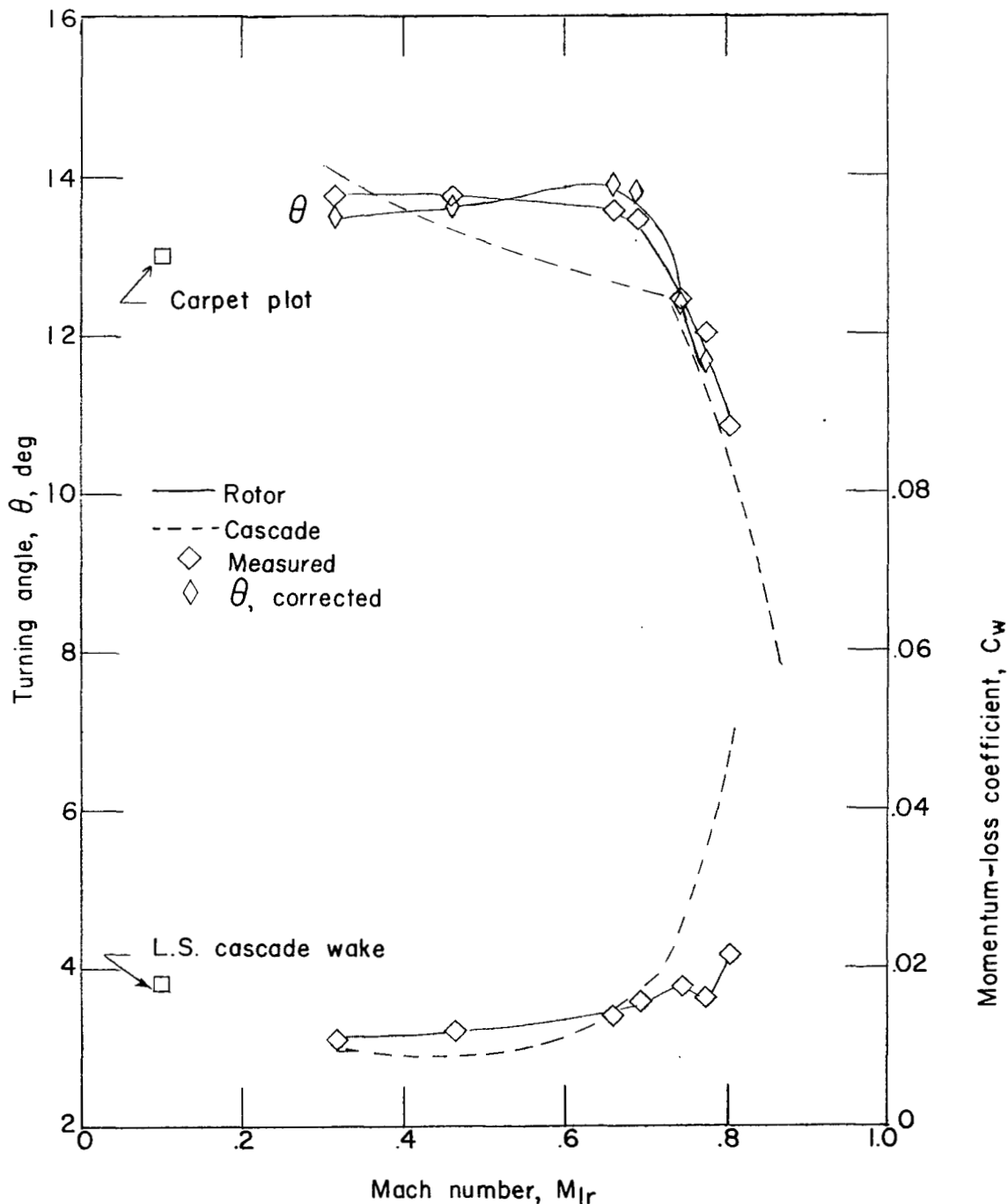
Figure 13.- Continued.





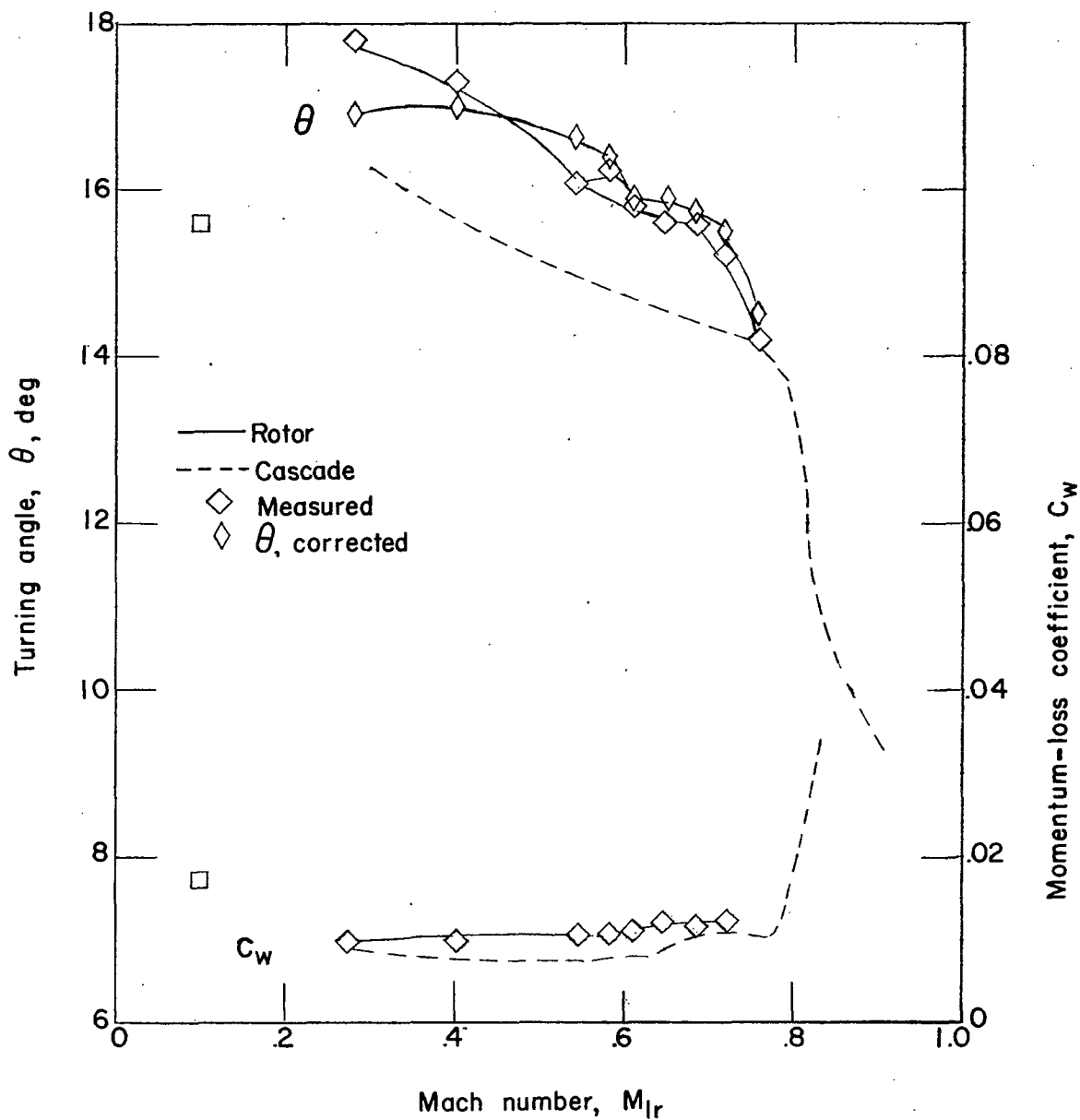
(c) Inboard section.

Figure 13.- Concluded.



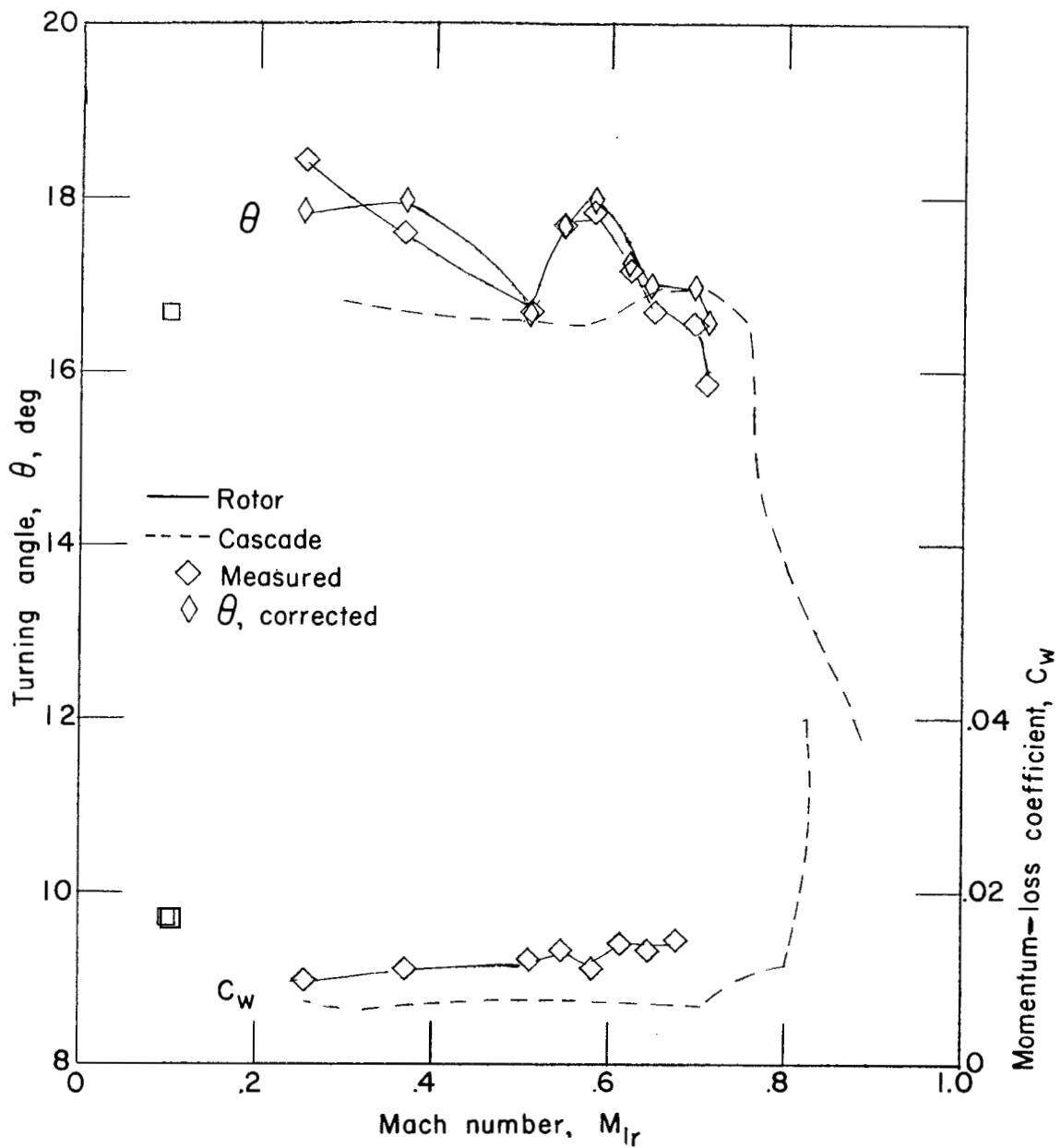
(a)  $\alpha = 7.4^\circ$ ;  $\beta = 55.5^\circ$ .

Figure 14.- Momentum-loss coefficient and turning angle with Mach number variation for the outboard section (NACA 65-(10.96A<sub>10</sub>)10).



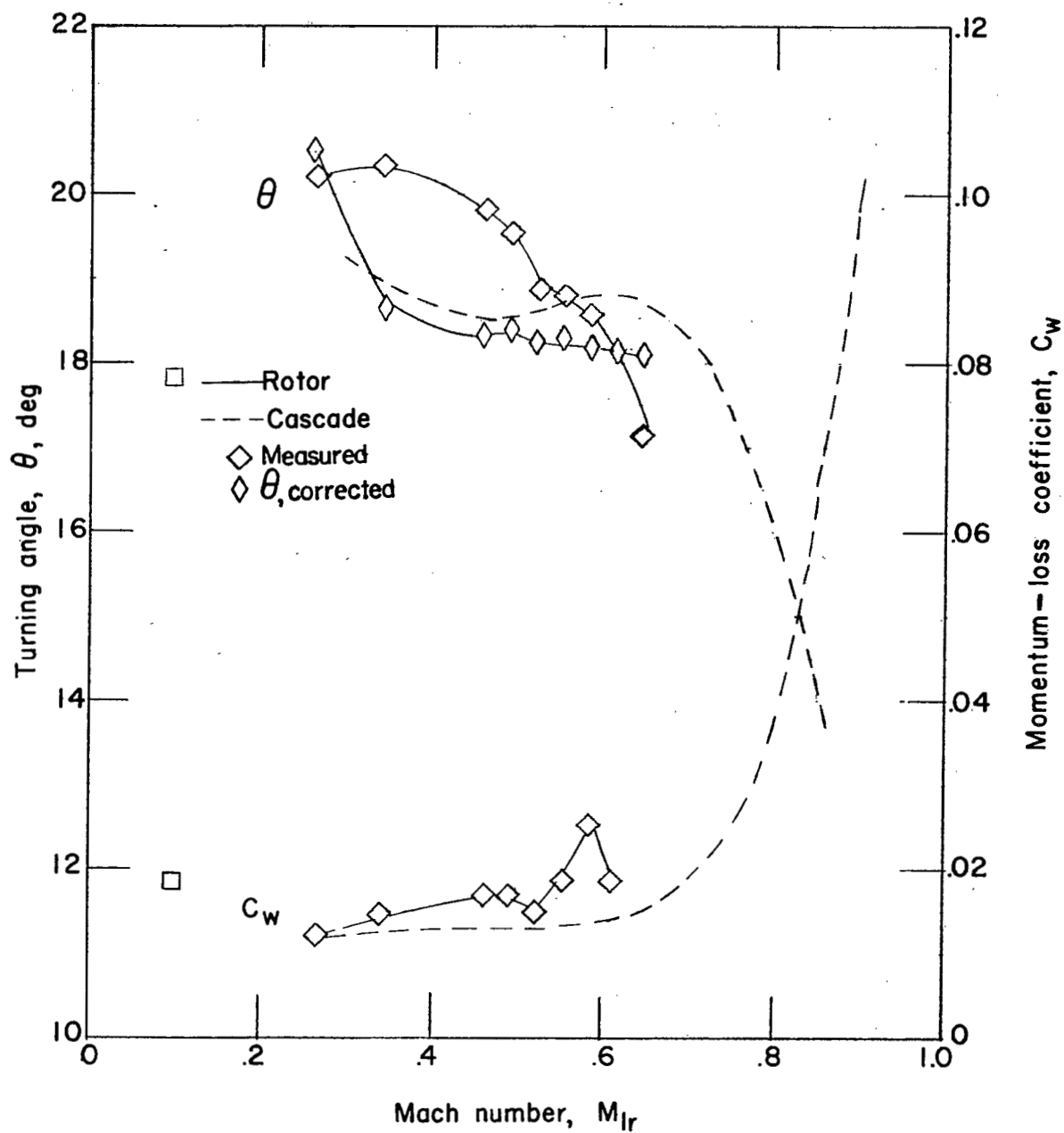
(b)  $\alpha = 10.9^\circ$ ;  $\beta = 59.0^\circ$ .

Figure 14.- Continued.



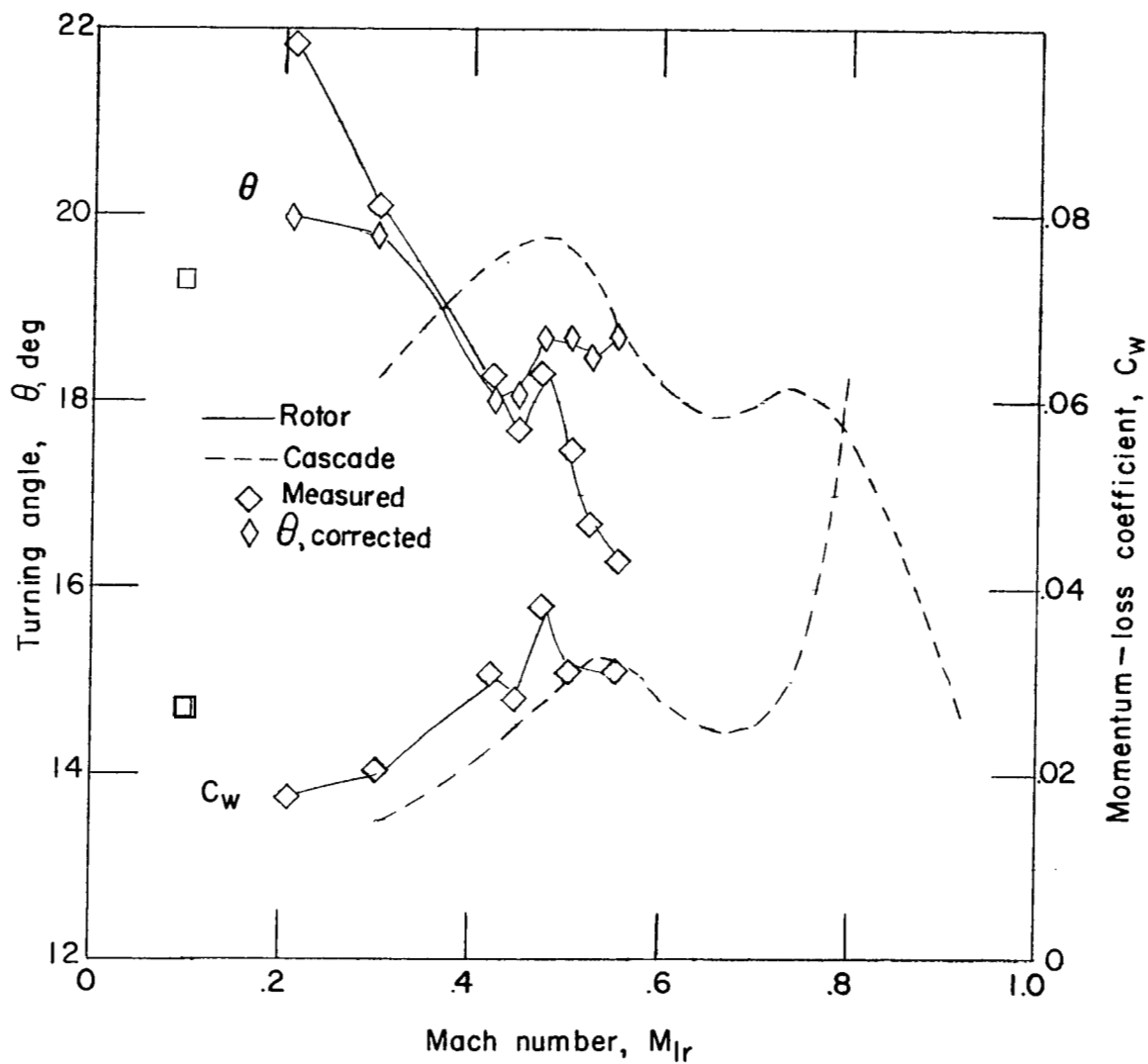
(c)  $\alpha = 12.4^\circ$ ;  $\beta = 60.5^\circ$ .

Figure 14.- Continued.



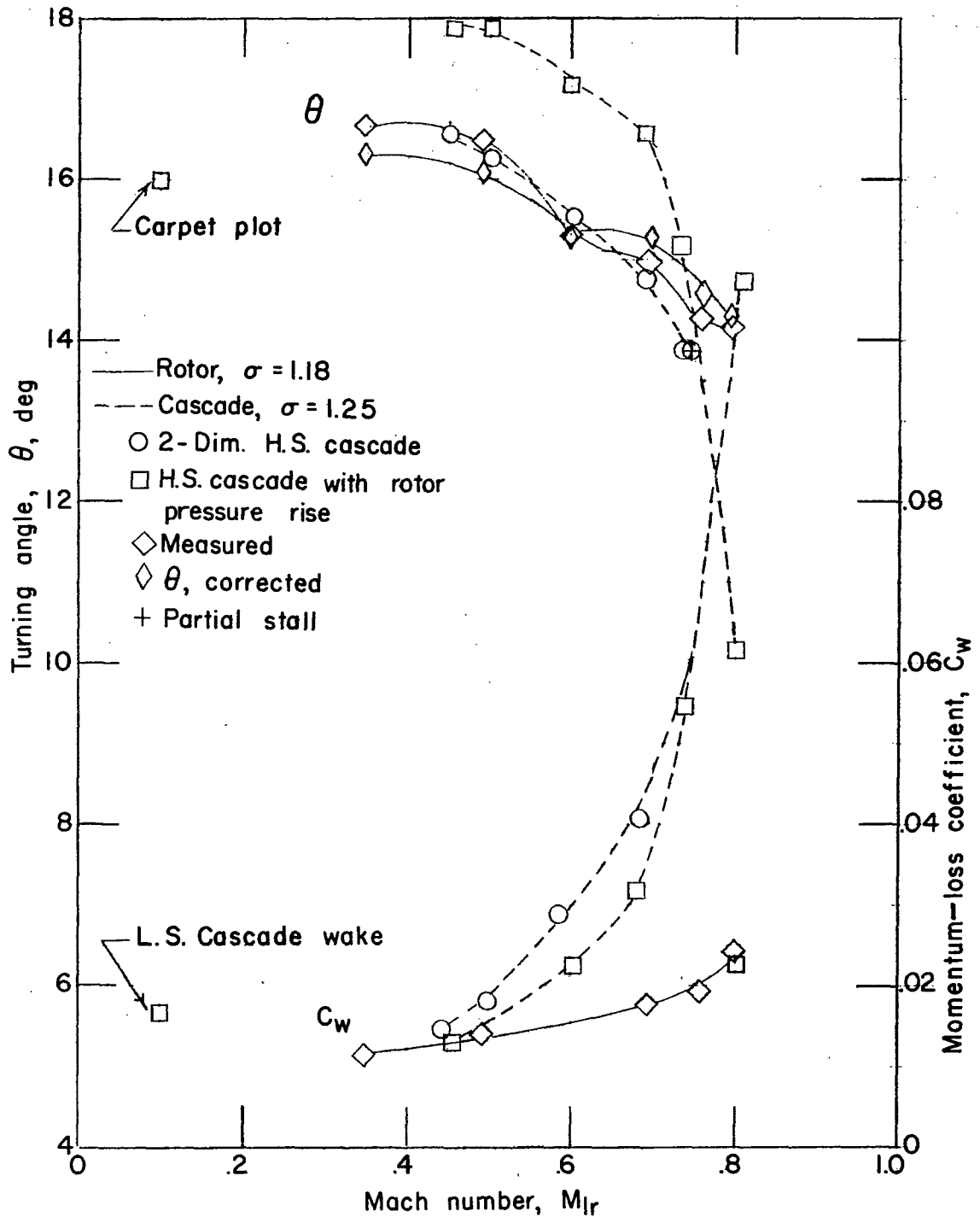
(d)  $\alpha = 14.3^\circ$ ;  $\beta = 62.4^\circ$ .

Figure 14.- Continued.



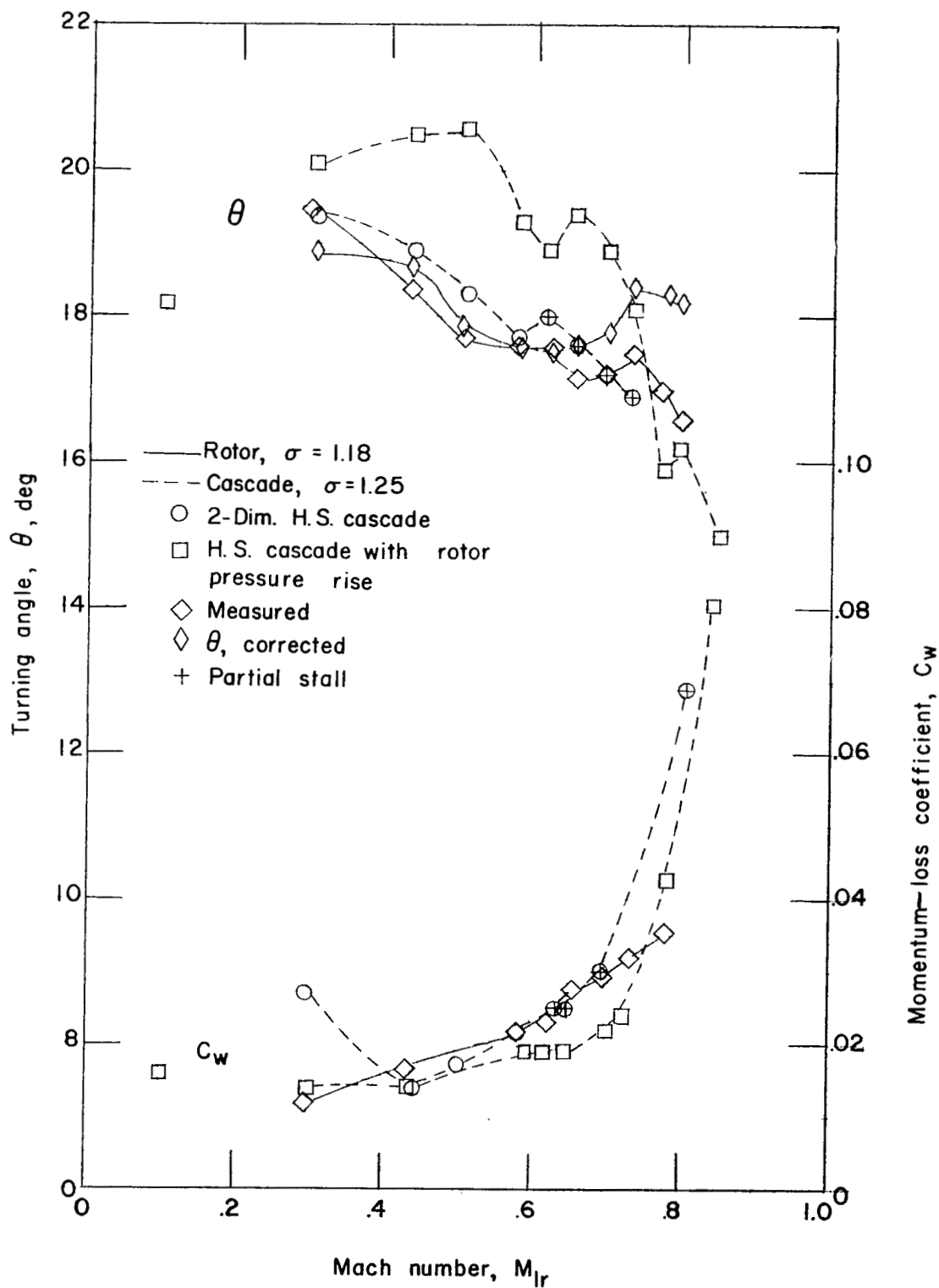
(e)  $\alpha = 17.3^\circ$ ;  $\beta = 63.4^\circ$ .

Figure 14.- Concluded.



(a)  $\alpha = 10.0^\circ$ ;  $\beta = 56.1^\circ$ .

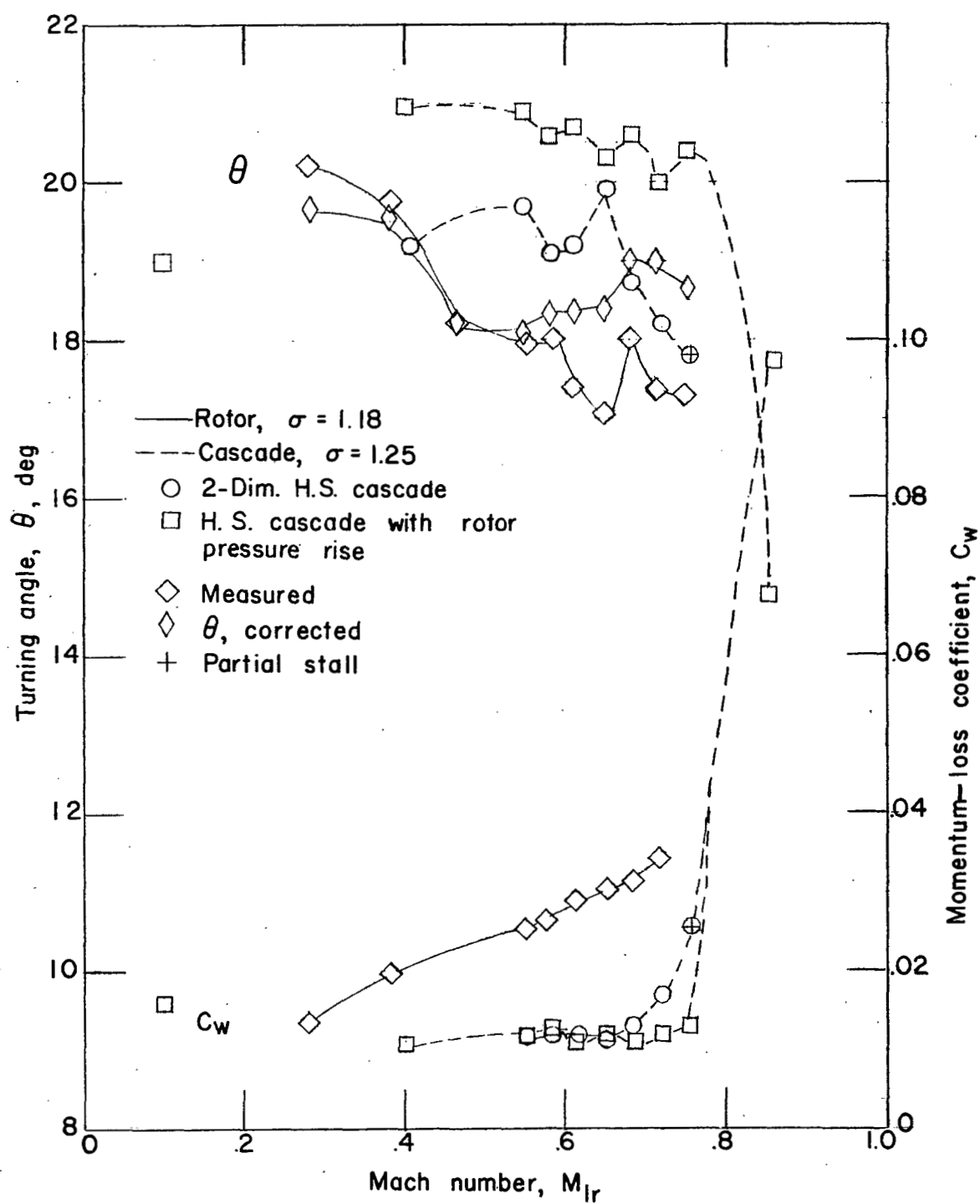
Figure 15.- Momentum-loss coefficient and turning angle with Mach number variation for the mean section (NACA 65-(12A<sub>10</sub>)10).



(b)  $\alpha = 12.7^\circ$ ;  $\beta = 58.8^\circ$ .

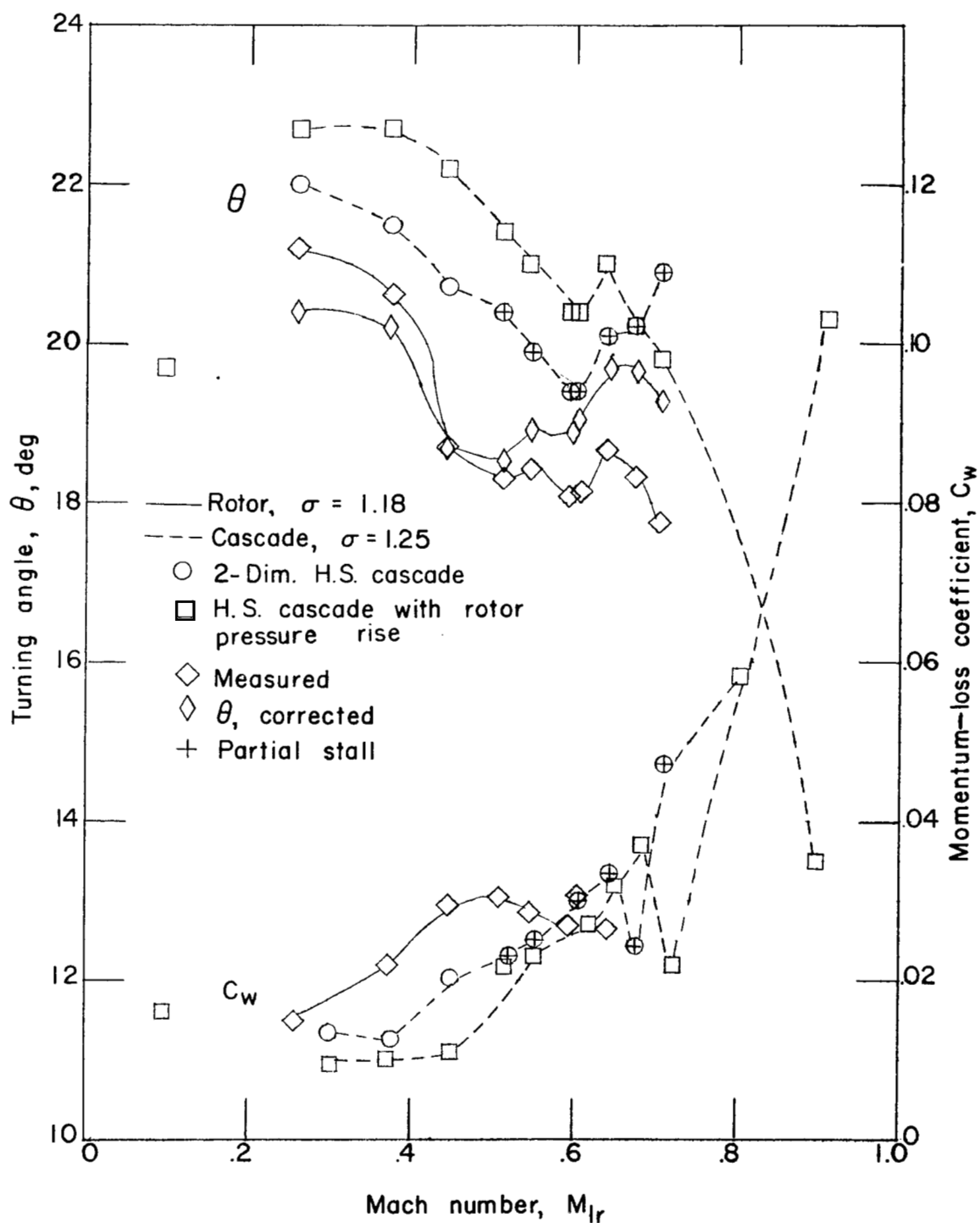
Figure 15.- Continued.





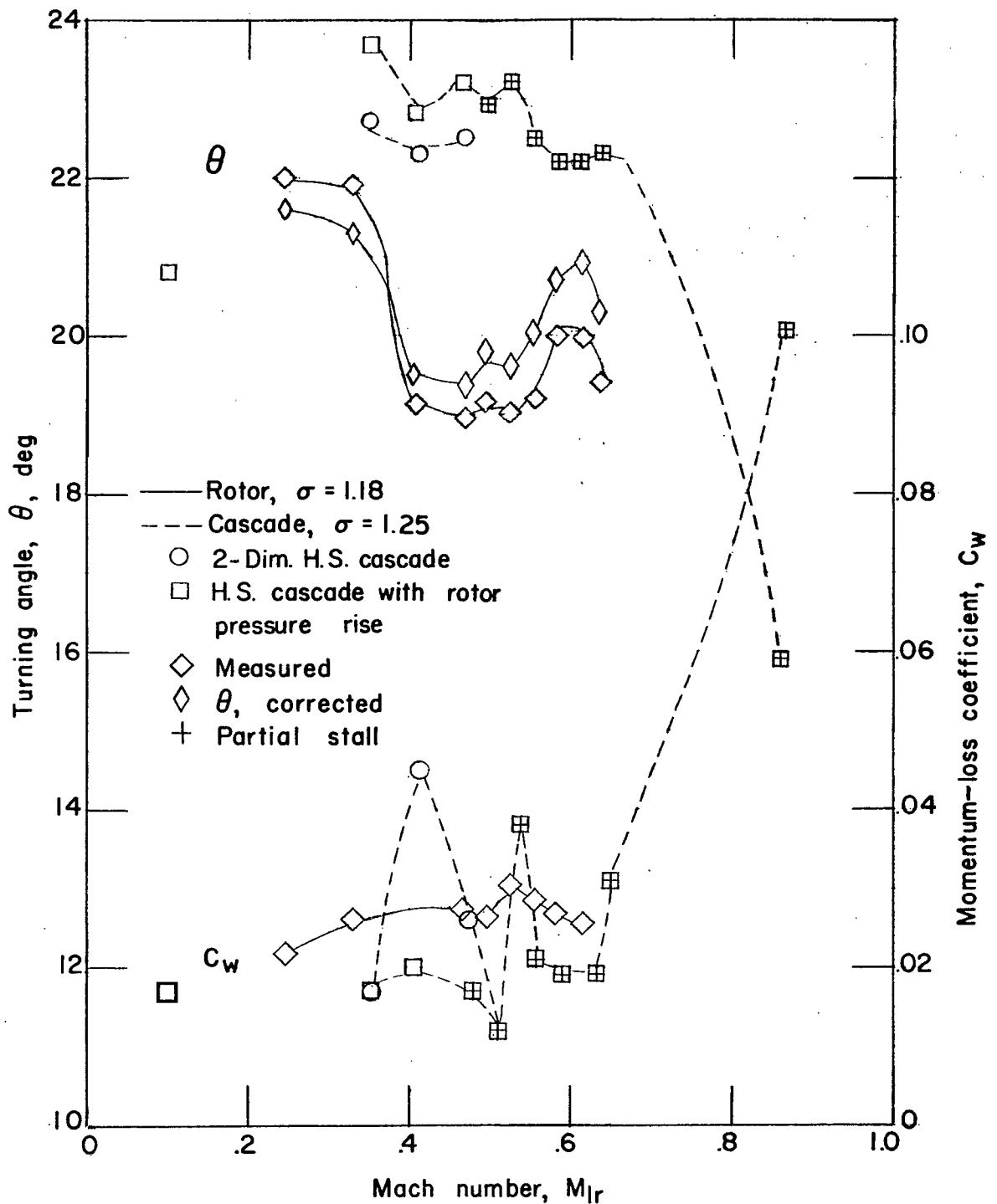
(c)  $\alpha = 13.8^\circ$ ;  $\beta = 59.9^\circ$ .

Figure 15.- Continued.



(d)  $\alpha = 14.8^\circ$ ;  $\beta = 60.9^\circ$ .

Figure 15.- Continued.



(e)  $\alpha = 16.8^\circ$ ;  $\beta = 62.9^\circ$ .

Figure 15.- Concluded.

NASA Technical Library



3 1176 01438 0399

**CONFIDENTIAL**